Teresa Brigitte Rieder, BSc

Construction and evaluation of an MRI-phantom to simulate typical tissue parameters

Master's Thesis

to achieve the university degree of

Master of Science

Master's degree programme: Biomedical Engineering

submitted to

Graz University of Technology

Supervisor Univ.-Prof. Dipl-Ing. Dr.techn.Rudolf Stollberger

Institute of Medical Engineering

Advisor: Dipl.-Ing. Andreas Lesch, BSc

Graz, January 2019

Statutory Declaration

I declare that I have authored this thesis independently, that I have not used other than the declared sources/resources, and that I have explicitly indicated all material which has been quoted either literally or by content from the sources used. The text document uploaded to TUGRAZonline is identical to the present master's thesis.

Date | Signature

Eidesstattliche Erklärung

Ich erkläre an Eides statt, dass ich die vorliegende Arbeit selbstständig verfasst, andere als die angegebenen Quellen/Hilfsmittel nicht benutzt, und die den benutzten Quellen wörtlich und inhaltlich entnommenen Stellen als solche kenntlich gemacht habe. Das in TUGRAZonline hochgeladene Textdokument ist mit der vorliegenden Masterarbeit identisch.

Datum | Unterschrift

Abstract

With the emerge of quantitative magnetic resonance imaging (qMRI) phantoms for quality assurance of quantification methods gain more and more importance. The purpose of this thesis were the construction and evaluation of such a phantom that provides verification of quantification methods with three different contrast types. Tissue-mimicking relaxation times were created with the doping of distilled water. As second contrast type different fat fractions ranging from 0 to 100%$_{vol}$ were created as emulsions of peanut oil and agarose gel. The last type adds to physiologically relevant relaxation times macromolecules that create a magnetization transfer (MT) effect to the phantoms. The created phantom was evaluated with respect to B_0 field homogeneity, B_1 field homogeneity, relaxation times, fat fraction and MT parameters.

Zusammenfassung

Mit dem Aufkommen von "quantitaive magnetic resonance imaging"(qMRI) werden Phantome zur Qualitätssicherung von Quantifizierungsmethoden immer wichtiger. Das Ziel dieser Arbeit waren die Konstruktion und Auswertung eines solchen Phantoms, das die Verifizierung von Quantifizierungsmethoden mit drei verschiedenen Kontrastarten ermöglicht. Gewebsähnliche Relaxationszeiten wurden durch die Zugabe kleiner Mengen paramagnetischer Substanzen zu destilliertem Wasser erreicht. Als zweite Kontrastart wurden Emulsionen mit Fettkonzentrationen zwischen 0 und 100%$_{vol}$ aus Erdnussöl und Agarosegel hergestellt. Bei der letzten Kontrastart wurden zu physiologisch relevanten Relaxationszeiten Makromoleküle hinzugefügt um einen Magnetisierungs Transfer (MT) Effekt hervorzurufen. Das hergestellte Phantom wurde im Bezug auf B_0 Feld Homogenität, B_1 Feld Homogenität, Relaxationszeiten, Fettkonzentrationen und MT Parameter ausgewertet.

Acknowledgment

First I would like to thank my supervisors Dipl.-Ing. Andreas Lesch, BSc and Univ.-Prof.Dipl-Ing Dr.techn Rudolf Stollberger for their support. They gave me important and inspiring feedback and shared their experience throughout the whole phantom development process.

Further I want to thank Ing. Walter Gmeindl for his great support with the fabrication of the phantom housing as well as Matthias Kainz from the Institute of High Voltage Engineering and System Performance for providing a desiccator for the evacuation of the magnetization transfer phantoms.

My thanks also go to my colleges Anna Seiwald and Seyda Agardan and Andreas Vorderleitner for the interesting discussions, their assistance in phantom mixing procedures and their support.

Additionally I want to thank my parents Klaus and Herta for giving me the opportunity to study and supporting me across the years.

x

Contents

List of Figures

1 Introduction

1.1 Quantitative MRI

In a classical point of view magnetic resonance imaging (MRI) is a non-quantitative imaging modality. The contrast is caused by a composition of multiple MRI relevant properties like longitudinal relaxation time (T_1), transversal relaxation time (T_2), proton density as well as the chemical environment of a proton and MT effects. The use of MRI for the quantification of single MRI properties can open up new possibilities for scientific and clinical applications. This implies a paradigmatic change from taking pictures to a process of measuring physical quantities - or from a qualitative to a quantitative point of view. There already have been several studies on how a quantification of T_1 or T_2 can be applied. Correlations with relaxation times and for example multiple sclerosis, epilepsy, dementia, alzheimer's disease and parkinson's disease have been shown and could be utilized for clinical monitoring or diagnosing. The measured quantities can also be referred to as quantitative biomarkers and may be for example tumour volume, functional network connectivities, metabolite concentrations, lung functions or fat fractions. The quantification of hepatic fat can be utilized for the diagnosing of nonalcoholic fatty liver disease (NAFLD) which has an increasing prevalence. Here the quantification of fat fraction can be a non-invasive alternative to the common biopsies. [1, 2, 3, 4, 5, 6, 7].

In order to provide quantitative imaging the results are expected to be reproducible over time, between subjects, between scanner sites and between manufacturers. To meet this requirement there is a need for standardized imaging protocols and data collections as well as suitable quality control. This is why phantoms with known MRI properties have been developed that facilitate the monitoring of reproducibility and also to provide accurate, always available and stable reference values for quantitative measurements [2, 8].

1.2 MRI Phantoms

MRI phantoms in general are objects with known geometry and imaging properties, like for example T_1 and T_2, that can be used as reference object for many quality assurance facets.
Quality assurance can be divided into two groups. Methods dealing with factors that rely on the imaging performance of the imaging device fall in the first group. These are factors like B_1 transmit and receive nonuniformity, B_0 nonuniformity, signal-to-noise ratio (SNR), image uniformity, gradient amplitude, geometric linearity, slice position and profile and high-contrast resolution. In order to ensure that the scanner is within specification these parameters shall be evaluated periodically. Often phantoms for this group are provided by vendors and quality assurance systems usually are included in service routines.
The second group deals with the quality assurance, validation and comparison of different quantification methods. Since these methods often are not provided by the magnetic resonance vendor (especially during fundamental research) a quality assurance system needs to be designed that meets the requirements of a particular quantitative measurement. These application-specific phantoms can not only be used for quality assessment but also for protocol-development or technologist trainings and corrections of already collected images. In fundamental research application-specific phantoms are used for the evaluation and validation of novel quantification methods [2, 8].

1.2.1 Commercially available phantoms

Phantoms that fall into the first group and hence allow the monitoring of general parameters regarding the physical performance are also called system-phantoms and are provided by several different organizations and companies as well as by MRI scanner manufacturers.
”The Phantom Laboratory” sells different imaging phantoms, including a couple of MRI phantoms under the name ”MAGPHAN”. They provide phantoms for the evaluation of gemoetric distortion, uniformity, slice thickness, resolution, SNR and T_1 and T_2 measurements [9].
”Leeds Test Objects” offers similar phantoms and further a reference phantom for diffusion weighted imaging [10].

The "National Institute of Standards and Technology" (NIST) has already done a lot of work in the field of qMRI, what includes the system-phantom "Phannie", that can be used for the analysis of geometric distortion, resolution, SNR, slice profiles and T_1, T_2 and proton density measurements. Additionally NIST provides more application-specific MRI phantoms like one for the evaluation of diffusion measurements, a susceptibility phantom and a breast phantom that includes sections for diffusion measurements as well as for T_1 and T_2 measurements [11, 12]. A phantom for quality assessment was designed by the "American College of Radiology" (ACR) and provides the evaluation of geometric accuracy, high-contrast spatial resolution, slice thickness, uniformity, signal ghosting and low-contrast object detectability [13, 14].

The available phantoms are often very expensive. The prices for the ACR phantom and Phannie are for example both of the order of 2000$ [15, 16]). Further for some applications (like fat fracion estimation) it is hard to find suitable commercially available phantoms.

1.3 About this thesis

The purpose of this thesis was the creation of a phantom to simulate several different MR properties in physiologically relevant value ranges. Three main types of phantoms were created. In order to have a reference for relaxation time mapping procedures the first type of phantoms are pure relaxation phantoms with as less disturbing effects as possible. These phantoms should imitate T_1 and T_2 of tissues. The second type are relaxation phantoms with MT effects and therefore, also include a variation of relaxation times but additionally should have a measurable MT-effect in a physiological range. This should reveal possible effects of MT on relaxation time measurements different from the gold standard methods inversion recovery and a sequence of spin echoes [17, 18]. The third type - fat-water phantoms - is a reference for fat fraction quantification. Different known mixtures of fat and water shall simulate fat concentrations in the human body in order to verify fat quantification algorithms.

After the creation of all mentioned phantom types they had to be evaluated with respect to their properties and also the housing of the phantom had to be evaluated with respect to it's influence on the measurements. Overall this means an evaluation of field homogeneities, relaxation times, magnetization transfer ratio, fat-water fraction with an IDEAL based algorithm [19] as well as with a spectroscopy method and the temperature dependence of relaxation times.

2 Methods

2.1 Phantom Manufacturing

2.1.1 General Phantom Design

The phantom in general was designed in a modular approach. It consists of contrast chambers which mimic different contrast properties that can be combined arbitrarily. According to this approach it is easy to extend the phantom hereafter with further contrast chambers with different properties. For each of the three mentioned phantom types there exist several contrast chambers in which the property that belongs to the phantom type is altered. In order to hold all contrast chambers in place and seal the phantom substances from the environment an appropriate housing had to be found.

Contrast Chambers

The first step for the design of the contrast chambers was to decide which material to choose in direct contact to the phantom substances. For that purpose different materials were considered.
Due to their susceptibility and conductivity non ferromagnetic metals were no option. Polymers were considered but also excluded since they have a permeability for gases and therefore, after some time air bubbles could arise no matter how properly the housings are sealed. Glass was then the material of choice since there is no permeability for gases and has relatively low impact on the magnetic field inside the MR scanner [20].
After the material was chosen two different designs of chambers were considered. The initial idea was to use ampoules. However, they only were commercially available in diameters up to 20mm and with very thin wall thickness and were therefore mechanically not very robust. As an alternative to the commercially available ampoules individual designs purchased at a

glassblower were considered but turned out to be a very expensive approach. The second design approach was the use of glass bottles with a standard taper grounded glass joint as closing system. Those grounded glass joints are also used in chemistry for airtight connections and to seal volatile substances from the environment. When grounded glass joints are greased they provide a hermetic seal [21]. Narrow neck glass bottles with conical shoulder were purchased at "Hecht-Assistent". The narrow neck was chosen to minimize the area at which the substances are potentially exposed to the environment. To prevent a large enough imaging area for each contrast chamber a volume of 50ml was sufficient (outer diameter: 42mm).
To reinforce the quality of the grounded glass joint seal the small gap between inner and outer joint was additionally sealed with an epoxy glue (Loctite 3430).
Further attention had to be taken when closing the bottles, since any trapped air needed to be avoided. Since the grease of choice (according to it's price) was vaseline, special care had to be taken on the temperature of the bottleneck when the joint was closed. Above a temperature of 37°C the vaseline starts to melt which leads to two problems. First, the phantom material is polluted and second the vaseline runs away from it's desired destination leading to a bad seal.
When closing the bottles with liquid content it appeared to be the best practice to let the inner joint slowly slide into the outer joint and then suck the remaining water in the gap with an absorbent towel. If the inner joint was pushed and twisted until the inner joint stuck firmly in the outer joint there was the risk that vaseline is pushed away from its designated place and therefore there cannot be provided a hermetic seal anymore.

Housing

Additionally to the contrast chambers a housing that holds the glass bottles in a defined position during a measurement was required. In order to improve the magnetic field homogeneity inside the phantom it was desired to design the housing in a way that it can be filled with water. This reduces susceptibility discontinuities between contrast chambers and the background. The influence of embedding media on the B_0 homogeneity is investigated in Section 3.1.1
The housing of the phantom can be seen in Figure 2.1 and the technical drawings are appended to this document (Appendix A). An acrylic glass

tube defines the overall shape of the housing, has a diameter of 180mm and hence, fits into a headcoil. Also the other parts of the phantom housing are made from acrylic glass. For the closure of the housing a bottom is glued into the tube. To hold the bottles in place there are eight drillings with a diameter that fits to the outer diameter of the bottles inside the bottom plate. The top plate can be clicked into the acrylic glass tube and is fixated with one plastic screw. For the purpose of making the housing water-proof an O-ring seals the gap between the acrylic glass tube and the top plate. For additional fixation of the bottles a layer of foam rubber is placed at the top of the bottles and holds them in place when the top plate is inserted and therefore pushes down the foam rubber. Since the top plate fits very tight inside the housing reopening could be very tough. For this purpose two rods were glued inside the acrylic glass tube, each below a drilling. When the housing has to be opened two screws can be screwed inside these drillings in order to press on the rods. This forces the top to lift up from its place inside the housing and it can be opened. To tighten the housing two short plastic screws with an O-ring also have to be screwed into these drillings. The drillings also have a further benefit. They can be utilized for the venting of the water filled housing to prevent susceptibility artefacts caused by trapped air.

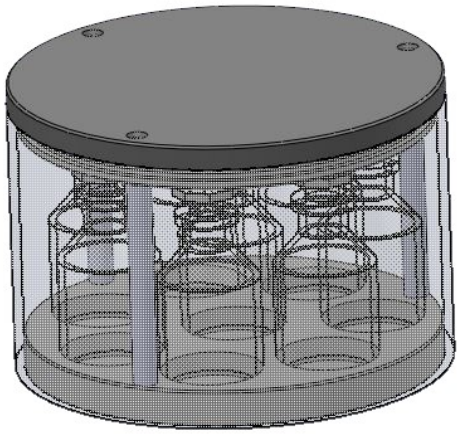

Figure 2.1: Phantom housing with used glass bottles inside

2.1.2 Degassification

In order to remove dissolved air from all phantom substances a degassification process had to be found. Two different degassing approaches were examined.

Ultra Sound

For liquid substances ultra sound degassification is very convenient. Two effects are responsible for the degassification which utilizes ultra sound for that purpose. The first is called ”gaseous acoustic caviation” and describes the diffusion of gas into near-vacuum bubbles that arise during the low pressure phase of an acoustic wave. These gas filled bubbles grow larger and larger in low pressure phase and extract the air from the surrounding liquid. The ”secondary bjerknes force” is the second effect and describes the attraction force that is experienced by two bodies that are pulsating with the same phase (like two bubbles pulsating in the same acoustic field). This means that two bubbles are accelerated against each other and can form even larger bubbles.
As soon as these two effects create bubbles that have a large enough buoyancy to rise to the surface of a liquid the gas can be released to the environment [22].

Vacuum

For the degassification of substances with high viscosity a different method than ultra sound has to be used since the rise of bubbles is more difficult in those substances, due to the high viscosity. The second approach was to evacuate a substance with dissolved gas in order to extract bubbles with the application of low environmental pressure.

2.1.3 Relaxation Phantoms

In literature one can find many different approaches on phantoms that simulate tissue-like relaxation time contrast [23, 24, 25, 26, 27, 28, 29]. Basically there exist two main types of relaxation time phantoms - gel-based

and water-based phantoms. The advantage of gel-based phantoms is the possibility to almost individually adjust T_2 by adding agarose to water. In order to avoid MT-effects, which are known to occure in agarose gels [30], it was decided to build water based relaxation phantoms. The MT-effect can distort the measurements of relaxtion times for some sequences. Furthermore water-based phantoms may have a longer durability [8]. To be able to adjust relaxation times nearly as flexible as with agarose one of the used substances needed to have a high impact on T_2 and a relatively low impact on T_1 at the same time. The substances used for modification of the water relaxation times were $Gd - DO3A - butrol$ and $MnCl_2$. Both of them were readily available for the project. $Gd - DO3A - butrol$ is a commonly used contrast agent (Gadovist) to reduce T_1. $MnCl_2$ fulfils the former mentioned criterion of a much higher impact on T_2 than on T_1 and therefore is suitable as a second component in order to be able to simulate a wide range of relaxation times [25, 31].

Doping of water

The relaxation times for undoped water are noticeably higher than typical relaxation times that can be measured for biological tissue (which can be seen in Table 2.1).

Table 2.1: Relaxation Times of Tissue at 3T [26, 32]

Tissue	T2 in ms	T1 in ms
Liver	42 ± 3	812 ± 64
Skeletal muscle	50 ± 4	1412 ± 13
Heart	47 ± 11	1471 ± 31
Kidney	56 ± 4	1194 ± 27
Cartilage 0°	27 ± 3	1168 ± 18
Cartilage 55°	43 ± 2	1156 ± 10
White matter	69 ± 3	1084 ± 45
Gray matter	99 ± 7	1820 ± 114
Optic nerve	78 ± 5	1083 ± 39
Spinal cord	78 ± 2	993 ± 47
Blood	275 ± 50	1932 ± 85
Fat	41 ± 0	385 ± 34

Hence, the relaxation times of water need to be shortened in order to use it as an appropriate phantom material. With the addition of substances like gadolinium, manganese, copper, nickel [33] or agarose [24] the relaxation times can be influenced according to Equations 2.1 and 2.2. Where r_1 and r_2 are the relaxivities of the added substance and C is the concentration of the influencing substance in water [25].

$$\frac{1}{T_1} = \frac{1}{T_{1,water}} + r_1 \cdot C \tag{2.1}$$

$$\frac{1}{T_2} = \frac{1}{T_{2,water}} + r_2 \cdot C \tag{2.2}$$

Since there are substances like manganese and agarose that mainly affect T_2 and substances that have a similar effect to both relaxation times (e.g. gadolinium, copper, nickel) it can be very useful to combine these two types of substances to be able to create T_1/T_2 combinations over a wide range. For the design of phantoms with (almost) arbitrary T_1/T_2 combinations made of two components a and b, where a is the substance that mainly affects T_2 Equations 2.3 and 2.4 are valid [24].

$$C_a = \frac{T_{2,desired}^{-1} - T_{2,water}^{-1} - (r_{2,b}/r_{1,b})(T_{1,desired}^{-1} - T_{1,water}^{-1})}{r_{2,a} - (r_{2,b}/r_{1,b})r_{1,a}} \tag{2.3}$$

$$C_b = \frac{T_{1,desired}^{-1} - T_{1,water}^{-1} - (r_{1,a}/r_{2,a})(T_{2,desired}^{-1} - T_{2,water}^{-1})}{r_{1,b} - (r_{1,a}/r_{2,a})r_{2,b}} \tag{2.4}$$

Physical effects

Physical effects that make a shortening of T_1 and T_2 possible are mainly dipole-dipole interaction, electron paramagnetism and scalar interactions. Due to their high susceptibility every contrast agent molecule acts as a magnetic dipole and can therefore be included in a mechanism called dipole-dipole interaction. Since every dipole has an dipole field they slightly affect the local B_0 field. If the dipole fields of two dipols are located close enough

to each other they have mutual influence. This field variation is called background field and varies randomly due to the presence of brownian motion. The amount of dipole-dipole interaction is coupled to parameters like the distance between spins or the gyromagnetic ratio γ.
Electron paramagnetism leads to strong relaxation centers close to paramagnetic atoms due to the high magnetic moment of their electrons. These relaxation centers also can increase the relaxation rates (and therefore decrease the relaxation times) of surrounding materials.
The third phenomenon is called scalar interaction. Here the relaxation is influenced by an indirect coupling between nuclei. Scalar interaction is also known as j-coupling and describes the splitting of resonance frequencies of nuclei into multiplets. The resulting phase shifts can lead to a shortening of T_1. [6, 34, 35].

Phantom Preparation

Eight phantoms with varying T_1 and fixed T_2 and eight phantoms with varying T_2 and fixed T_1 were created as relaxation phantoms. The chosen relaxation times that lie in a physiological range for 3 Tesla measurements can be seen in Table 2.2.

Table 2.2: Adjusted Relaxation Times for the T_1 and T_2 phantoms

Phantom Nr.	1	2	3	4	5	6	7	8
T1 in ms	200	400	600	800	1000	1200	1400	1600
T2 (fixed) in ms	165							
T2 in ms	30	65	90	115	140	165	190	215
T1 (fixed) in ms	440	800						

To calculate the necessary concentrations of $Gd-DO3A-butrol$ and $MnCl_2$ Equations 2.3 and 2.4 were applied. To increase the accuracy in dimensioning the amount of needed doping substances, the relaxivities of the used

doping substances had to be examined. The according measurement procedure can be found in Section 2.2.3. T_1 as well as T_2 of the distilled water ($T_{1,water}$ and $T_{2,water}$) that was going to be used for the preparation of all phantoms were measured. The result of this measurement also was used for the calculation of the needed doping agent concentrations (see Equations 2.3 and 2.4). With the given substances not all T_1/T_2 combinations are possible to achieve, since each doping agent has influence on both relaxation times. Mathematically some combinations would lead to negative concentrations, which cannot be realized in real world applications. Hence, limitations in the distance between T_1 and T_2 are present. Thus, it was not possible to create a phantom with T_2 = 30ms and T_1 = 800ms and consequently the chosen longitudinal relaxation time for that phantom was shortened in order to be able to simulate small physiologically relevant T_2.

Since very low concentrations of each doping agent have a high impact on the relaxation times, diluted stock solutions (31.26 mM for $MnCl_2$ and 20mM for $Gd-DO3A-butrol$) were prepared in order to minimize measurement errors when pipetting the doping agents. The stock solutions' relaxivities were evaluated before the phantom creation as it can be seen in Section 2.2.3.

For each phantom the calculated amount of each doping agent stock was pipetted into 75ml distilled water. The mixture was then filled into a glass bottle (see Section 2.1.1) and placed in an ultrasound bath at a temperature of 70 °C for 90 minutes. Occationally (approximately every 30 minutes) the ultrasound bath was switched off and on in order to let the created air bubbles escape more easily. The temperature of 70°C was chosen since liquids can dissolve less gas at higher temperatures [36] and therefore the degassification process is supported. The bottles then were cooled to a temperature of 25°C in a water bath before they were carefully closed with their plugs and vaseline. Subsequently the gap between plug and bottle was dryed with an absorbant towel and the bottles were sealed with Loctite 3430 and immediately stored at the MRI-Scanner room. This location has an ambient temperature of 23°C that can be considered as constant. Here the water shrinks slightly due to a temperature decrease with respect to the 25°C when closing the bottles and the plug is sucked into the bottles more tightly before the sealing glue fully cures. A storage at constant temperature is very important after the glue cured since then the density variations of the liquids cannot be compensated by the plug's elasticity any more. The effect

of a small temperature change between 20°C and 25°C are investigated below.

Some of the bottles showed leaky spots due to inefficient closing or air-bubbles due to inefficient degassification after a few days. In that case a smaller amount of phantom dilution was prepared (e.g. 5ml) and used for topping up the phantom after reopening. To be able to create a tight seal after reopening the plug has to be cleaned properly before closing. This was done by ultrasonication for 5 minutes at 70°C.

Water Volume Calculation with varying Temperature

Following values for the density of distilled water were gathered from [37]. The volume at 25°C is estimated for a completely filled bottle.
$\rho_{20C} = 0.998203 \frac{g}{ml}$
$\rho_{25C} = 0.997044 \frac{g}{ml}$
$V_{25C} = 60ml$

$$m = V_{25C} \cdot \rho_{25C} = 59.823g \tag{2.5}$$

The mass stays constant with a temperature fluctuation so the volume with an other density can be calculated.

$$V_{20C} = \frac{m}{\rho_{20C}} = 59.931ml \tag{2.6}$$

$$\Delta V = V_{25C} - V_{20C} = 69.5\mu l \tag{2.7}$$

If the bottle neck is observed the shape of the calculated volume can be considered as a cylinder with a radius r of 7mm. Therefore the change of water level Δh can be calculated as follows.

$$\Delta h = \frac{\Delta V}{r^2 \pi} = 0.455mm \tag{2.8}$$

This means that a reduction of temperature from 25°C to 20°C to a shrinkage of water by 69.5µl which is a macroscopically visible volume or an equivalent

decrease of water level in the bottle neck of 0.455mm.

2.1.4 Fat-Water-Phantoms

In different tissues different ratios of fat and water can be found. The quantification of fat ratio can be a powerful indicator for pathologies like NAFLD. Non invasive magnetic resonance quantification methods are a promising alternative to nowadays mainly used biopsies [7]. In order to have a reference object for fat quantification methods in magnetic resonance imaging a set of fat-water phantoms was created.

Emulsions

An emulsion consists of two immiscible liquids. One of the liquids is called continuous phase and one disperse phase. The disperse phase forms droplets that are surrounded by the continuous phase. To be able to form an emulsion an additional substance has to be added to the two immiscible liquids which is called emulsifier. As emulsifiers often surfactants are used. These molecules have a hydrophilic and a lipophilic part. With this property they are able to bind to the oil phase as well as to the water phase and enable the mixing of two immiscible liquids. An appropriate emulsifier alone is usually not enough to prevent an emulsion from a breakdown in the long term. There are different types of breakdown processes shown in Figure 2.2 [38, 39].

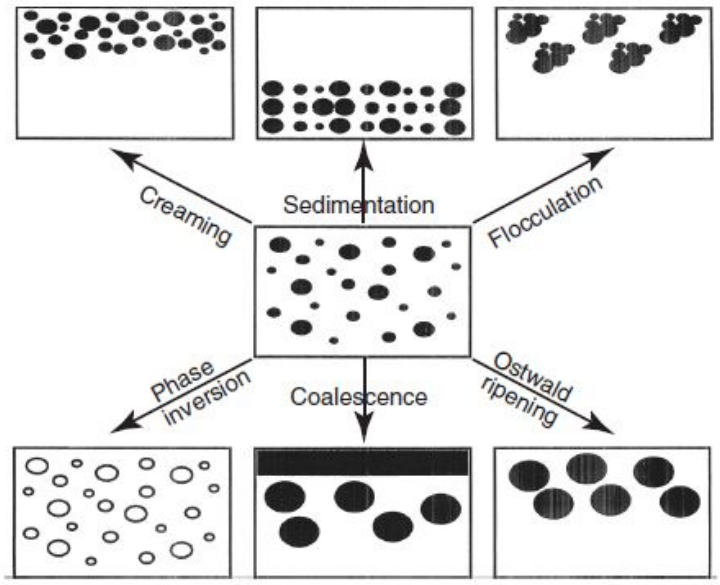

Figure 2.2: Differnt types of emulsion breakdown processes [38]

To prevent an emulsion from these breakdowns various precautions can be taken. The most relevant precautions for the created phantoms are the following:

- Reduce the droplet size
- Use thickeners to increase the viscosity of both phases
- Use mixed surfactant films

Homogenization

To take the first precaution - reduce the droplet size - devices called homogenizers can be utilised. Homogenizers are devices that produce high shear stresses in immiscible liquids in order to decrease the droplet sizes as well as to make sure that the two liquids are equally distributed in the volume. In Figure 2.3 a rotor-stator mixer is sketched, where a high speed rotor is surrounded by a stator and the gap between the two components is as small as possible. When the emulsion is forced to go through the thigh

gaps between rotor and stator very high shear stresses are applied to the liquids which break up large droplets [40].

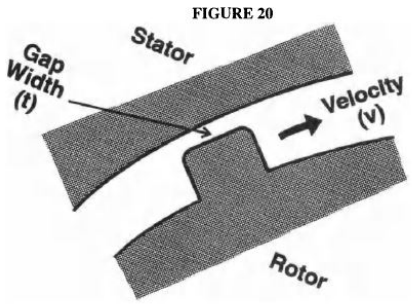

Figure 2.3: Sketch of a high shear mixing device in order to reduce droplet sizes in emulsions [40]

For the creation of an homogeneous emulsion that also provides homogeneous MR-images high shear stresses had to be applied to the emulsion as mentioned previously. First attempts with manually mixing the emulsion with available tools like spoons failed. The disperse and continuous phase could be seen in the images. For a good emulsification a homogenizing device was required and therefore a homogenizer similar to the rotor-stator mixer was constructed. Additionally the application of a rotor stator mixer increased the stability of the emulsion since small droplet sizes are one criterion for stable emulsions.

High shear mixing attachment

The approach of a high shear mixer was suitable since a stepper motor was readily available for this project. Inspired by the sketch that can be observed in Figure 2.3 a high shear mixing attachment for the available steppermotor was constructed with Solid works and afterwards 3D-printed with the xyz-Printer DaVinci Pro Jr.. The construction can be seen in Figure 2.4. Technical drawings can be gathered from the Appendix B.

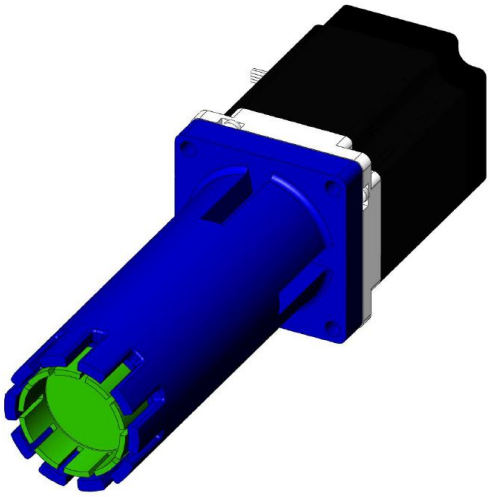

Figure 2.4: 3D printed high shear mixing attachment with stepper motor

Motor Control Unit

To run the stepper motor a suitable control unit had to be found. An output stage for stepper motors also was readily available. To run this output stage a square-wave signal had to be generated and fed to the output stage. For the generation of this signal a small circuit was designed and cased in an 3D-printed housing. The schematics, layout and also the technical drawings can be found in the Appendix B

Phantom Preparation

The contrast chambers of the fat-water-phantom consist of emulsions with different fat-water concentrations between 0 and 100%$_{vol}$. For the water phase distilled water's relaxation times were adjusted with Gd-DO3A-butrol and agarose to a biologically relevant range. Agarose also acts as an soldifying agent in the emulsion since it increases the viscosity of the water phase when cooled down. As an emulsifying agent sodium dodecyl sulfate (SDS) was used which can also be found in literature in fat-water phantom recepies [7, 41, 42]. SDS is an anionic surfactant and is often used in cosmetics like shampoo and dental creams [39].

For the fat-phase peanut oil was used which has similar MRI properties than human adipose tissue [43]. The ingredients described so far in principle can form a stable emulsion already. According to fact that the whole range of fat-water concentrations had to be covered not all emulsions were properly soldified since high fat concentrations cannot be gelled with agarose. To deal with this issue 10% stearic acid was added to the peanut oil which soldifies the fat phase at room temperature. An additional advantage of the addition of stearic acid to the fat phase is the fact that stearic acid is a nonionic surfactant and therefore improves the emulsion since the mixture of ionic and nonionic surfactants can often increase the stability of emulsions [39, 38].
As a preservative sodium benzoate (3mM) was added [44].

Mixing procedure

For the emulsion creation first water- and fat-phase were prepared for all 11 phantoms. In total water and fat phase were created at a volume of 550ml each. Therefore an agarose gel with 2.57 $\%_{mass}$ agarose powder was created for the water phase. The agarose powder was slowly added to distilled water at room temperature while slowly stirring with a magnetic stirrer. The agarose mixture was allowed to swell for 30 minutes. Then the agarose mixture was slowly heated up on a heating plate with occasionally stirring until the agarose was completely diluted. Then 43 mM SDS, 103.5 mM Gd-DO3A-butrol and 3 mM sodium benzoate were added. The finished water phase was stored in an ultrasound bath at 70°C for degassing.
The fat phase consisted of peanut oil (which was weighted with knowledge of it's density) with $10\%_{vol}$ of stearic acid. Stearic acid was added to the oil and the mixture was heated with occasionally stirring until the stearic acid was completely dissolved. The fat-phase was stored in the ultrasound bath as well.
The two phases were then mixed with the homogenizer (see Figure 2.4) in different concentrations between 0 and $100\%_{vol}$ with intervals of $10\%_{vol}$. The rotational speed of homogenization was decreased with increasing fat concentration in order to prevent the emulsions from foaming. The volumes of water- as well as fat-phase were weighted with knowledge of the densities of each component in the phases. This was found to be a more accurate method than measuring the volume directly. During the preparation process the actually weighted mass was noted to calculate the

real fractions. The emulsions were stored in an ultrasound bath at 70°C for one hour with occasional stirring. Subsequently they were filled into the glass bottles and stored in the ultrasound bath for another hour without further heating. Afterwards they were kept in the fridge until they solidified (approximately one more hour). Since the emulsions shrank when cooling down they needed to be topped up before closure. For the topping up remaining emulsions were stored in 10ml vials in the ultrasound bath at 70°C until the according phantoms solidified.

2.1.5 Magnetization Transfer Phantoms

The protons that can be imaged in tissue are bound in different chemical environments. The more mobile protons are the longer is their T_2. Hence, protons of macromolecules have very short T_2 and therefore cannot be detected directly with a magnetic resonance scanner. Nevertheless they can be made visible with an offresonance radio frequency(RF)-impulse. As it can be seen in Figure 2.5 macromolecules are much more sensitive to offresonance RF-impulses than mobile protons. If this offresonance RF-impulse is applied as a saturation pulse the immobile protons are saturated. The mobile protons are influenced indirectly by the saturation pulse since there is an exchange between both types - magnetization is transferred from the immobile protons in large molecules to the mobile protons in small molecules and vice versa. The visible effect in resulting images is a signal decrease depending on the amount of macromolecules in a voxel and their exchange rates. This imaging modality is known as magnetization transfer contrast (MTC) [45].
The magnetization transfer phantoms were created in order to have an additional phantom for relaxometry with biologically relevant MT.

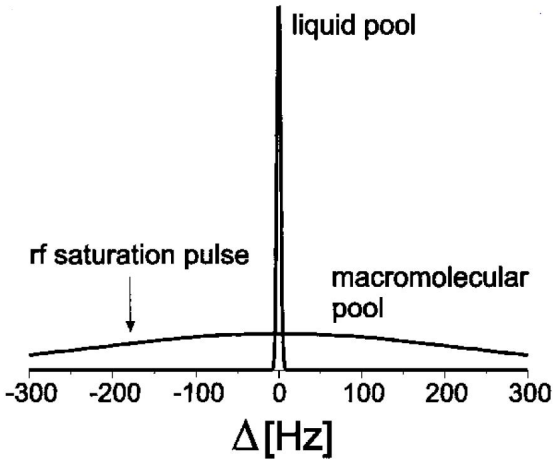

Figure 2.5: Absorption linshapes of the macromolecular pool (immobile protons) and the liquid pool (mobile protons). An offresonance rf saturation pulse as marked is only noticeable for the macromolecular pool.[45]

Macromolecules for the Simulation of Magnetization Transfer

To simulate MT properties of tissue macromolecules are needed in the phantom substance. In previous works cross-linked bovine serum albumin already has been described as a model for tissue [46]. Also large sugar molecules like agarose can be a substance to increase the magnetization transfer effect in substances. Though in comparison with cross-linked proteins like bovine serum albumin it can be seen that bovine serum albumin behaves more similar to human tissue than agarose and therefore should be preferred for the created phantoms [30]. Cross-linking is a reaction where proteins are linked to each other and therefore form even larger molecules - the magnetization transfer effect is increased. This reaction can be initiated chemically (addition of glutaraldehyde [46]) or thermically (apply heat to the substance [47]).
Due to the high cost of bovine serum albumin an alternative with similar properties was searched. The idea was to use an other subtype of albumin. Ovalbumin is albumin extracted from egg-white and can be purchased in a raw form (approximately 80% purity) for a distinctly lower prize.

Phantom Preparation

For the MTC chambers eight phantoms were created which were adjusted to different relaxation times (see Table 2.3) and an MT-effect as similar to tissue as possible. For the MT-effect some initial experiments were executed and $33\%_{mass}$ ovalbumin was found to create a magnetization transfer effect similar to tissue. The related measurement are described in Section 2.2.5.

Table 2.3: Adjusted Relaxation Times for the Magnetization Transfer Phantoms

Phantom Nr.	1	2	3	4	5	6	7	8
T1 in ms	350	500	650	800	920	200	200	200
T2 (fixed) in ms	40	40	40	40	40	20	30	35

In order to create the phantoms 600ml protein dilution with $30\%_{mass}$ ovalbumin had to be created. Ovalbumin has to be added very slowly to water to prevent it from forming lumps. The best practice for this dissolving process was found to be a combination of slow mixing with a magnetic stirrer and dispensing the ovalbumin in small portions over the water surface with a spatula. The subsequent portion was added as soon as the previous was diluted completely. As a preservative also in MT phantoms sodium benzoate (3mM) was added.
For the adjustment of relaxation times the mixed stocks of Gd-DO3A-butrol and $MnCl_2$ were used again and their needed concentrations were calculated using Equations 2.3 and 2.4. To apply the formulas correctly for the magnetization transfer phantom T_1 and T_2 of the raw ovalbumin dilution was measured and used as $T_{1,water}$ and $T_{2,water}$ respectively.
Since foaming could not be prevented completely a degassing method for the ovalbumin dilutions had to be found. It was found that the best practice is to evacuate the phantom substances for multiple cycles of 15 minutes with intermediate stirring to prevent the substance's surfaces from becoming too dry. After this procedure the phantoms were filled into a glass bottle and stored in the fridge overnight to let the last remaining air bubbles escape.
Then the proteins were cross-linked. Therefore, the glass bottles were heated in a water-bath at 85°C for 10 minutes. The bottles with the gelled dilutions were then closed and sealed.

2.2 Measurements

2.2.1 B_0 Homogeneity Measurements

The homogeneity of the main magnetic field is an important factor for the imaging quality that can be reached in an MRI scanner. There are two artifacts that can occur due to magnetic field inhomogeneities. The first is image distortion. This is due to a misregistration to a spatial position since the spatial encoding is done by gradients. The other one is called echo shifting. This means that a gradient echo (GRE) occures on a shifted echo time T_E' and hence a signal loss may be observed when the echo is recorded at echo time T_E [48, Chapter 20.0].
For MRI sequences that are based on GRE methods it is additionally relevant that additional inhomogeneities have an influence on T_2^* measurements since they lead to a shortening of T_2^*.

How Inhomogeneities influence T_2^*

In general T_2 is shortened by additional spin dephasing due to B_0 inhomogeneities. If the precession frequency of two spins in the same voxel only differs by 5 Hz after 100 ms the slower spin will be half a turn (180°) behind the faster spin and therefore their signals will cancel out each other. The consequence will be a decay in signal. According to Equation 2.9 the precession frequency ω is proportional to the magnetic field B and the gyromagnetic ratio γ of hydrogen nuclei and will adapt to a change in the magnetic field.

$$\omega = \gamma \cdot B \tag{2.9}$$

If Lorentzian spectral density functions are assumed the reduced transversal relaxation time can be stated as it can be seen in Equation 2.10 where $\frac{1}{T_2'}$ is $\gamma \Delta B$ [49].

$$\frac{1}{T_2^*} = \frac{1}{T_2} + \frac{1}{T_2'} \tag{2.10}$$

Field Map Collection

In GRE imaging B_0 inhomogeneities have impact on the resulting images in two ways. The first is - as already mentioned - the faster signal decay with the time constant T_2^* due to local field inhomogeneities inside one voxel. The second impact is caused by global inhomogeneities of B_0 that result in phase shifts across the whole image, due to the different resonance.
By averaging the fundamental relation between main field and frequency (see Equation 2.9) Equation (2.11) for the B_0 inhomogeneity can be derived out of two GRE acquisitions. [50]. The phase difference $\Delta\phi$ can be gathered by the subtraction of the phase images of two echo gradient images with different echo times TE_1 and TE_2.

$$\Delta B_0 = \frac{\Delta\phi}{\gamma(TE_2 - TE_1)} \tag{2.11}$$

Image Acquisition

A Skyra 3T system (Siemens, Erlangen, Germany) was used to acquire four 2D GRE images (Echo Time (TE) = [2.25ms, 5.57ms, 8.89ms, 1220ms]). Repetition Time (TR) was 60ms for all images and flip angle α was 30°. 256 x 256 voxels were recorded in a field of view (FoV) of 180 x 180mm with 3mm slice thickness.

Glass Bottle Evaluation

To investigate the influence of the selected glass bottles on the B_0 homogeneity Equation 2.11 was applied on the two GRE images with TE 2.25ms and 8.89ms.
A single bottle has been recorded in coronal and sagittal direction. To see if neighbouring bottles influence each other in terms of B_0 field homogeneity, we also acquired two bottles simultaneously in different arrangements. First they were arranged horizontally next to and then vertically above each other. The bottles were oriented along the main magnetic field(see Figure 2.6).

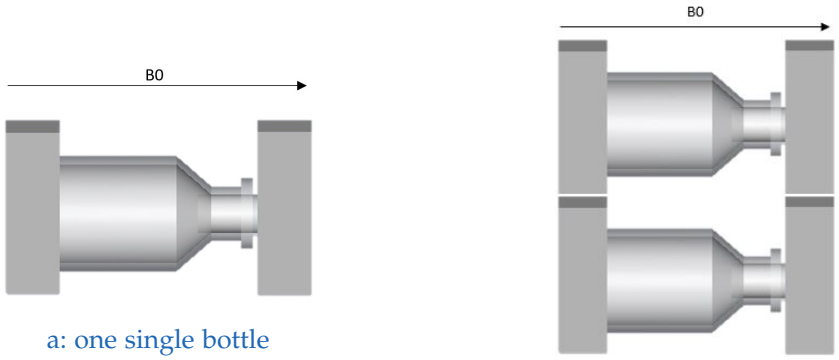

a: one single bottle

b: two stacked

Figure 2.6: Configurations of bottles in the MRI-Scanner for glass bottle evaluations with respect to B_0 homogeneity

Phantom Housing Evaluation

To evaluate the homogeneity of the whole created phantom eight water based phantoms were put into the water filled housing and the whole housing was placed inside the head coil of the scanner so that the phantoms were oriented as sketched in Figure 2.6(a). To evaluate the homogeneity of the whole housing the four GRE acquisitions were recorded for a 3D-volume with 32 slices of 2mm thickness. In each slice 128 x 128 voxels in a FoV of 185 x 185mm were recorded.

Data Processing

Glass Bottle Evaluation

Before $\Delta\phi$ can be computed it has to be considered that there will be wrapped phases in the phase map. This is due to the fact that the phase represents a rotation which is 2π periodic. As a consequence the phase is represented in an interval between $-\pi$ and $+\pi$. If the interval is exceeded the value jumps to the opposite site of the interval similar to a modulo operation. The resulting jumps in the phase maps need to be compensated before the two recorded phase maps can be subtracted. Methods that implement such compensations are called phase unwrapping methods [51]. Therefore an online available matlab script was used which implements the

phase quality guided phase unwrapping method [52].
ΔB was then calculated as stated in Equation 2.11. For better comparability ΔB was rescaled to ppm as it is stated in Equation 2.12 with B_0 set to $2.895T$ since this is the magnetic field strength of the used magnet. ΔB was also rescaled to frequency in order to see how precession frequency is influenced by B_0 inhomogeneities as stated in Equation 2.13

$$\Delta B_{ppm} = \frac{\Delta B \cdot 10^6}{B0} \tag{2.12}$$

$$\Delta f = \frac{\Delta B \cdot \gamma}{2\pi} \tag{2.13}$$

To compare the homogeneity variations a region that seemed to be homogeneous was selected and ΔB_0 was evaluated for each bottle configuration. In Figure 2.7 the selected region is displayed. In order to ensure that the same region is selected for each bottle configuration - which implies that the different bottle configurations can be properly compared to each other - the B_0 maps of all configurations were registered on each other.

Figure 2.7: Region selected for evaluation of the influence of neighbouring bottles

This analysis is influenced by eddy currents which are induced in the beginning of each measurement and diminish with time. Due to this influence there can be observed differences in the fieldmap amplitude when different echo times are utilized for evaluation.

To overcome this issue an alternative evaluation technique was used. For the utilized modified IDEAL [19] evaluations (see Section 2.2.4) a field map is estimated from all input images and can also be used for that purpose. In this estimation more than two images are taken into account and the eddy currents' influence is minimized due to an averaging of four measurements. An additional advantage of this evaluation is a smoothness constraint in the estimation algorithm that reduces noise that might influence the quality of the fieldmaps.

To have a further insight on how the measurement quality can be affected by magnetic field inhomogeneities the change of T_2^* caused by inhomogeneities was investigated. The maximum ΔB in each voxel of 1mm x 1mm x 4mm was used to find the maximum T_2^* where the additional influence of B_0 inhomogeneities shortens T_2^* by less than 10% according to Equation 2.10.

Phantom Housing Evaluation

To result in a fieldmap from the acquired data also for the whole housing the B_0 estimation implemented in the IDEAL algorithm was utilized. Further the influence on T_2^* measurements was evaluated according to Equation 2.10

2.2.2 B_1 Homogeneity Measurements

Also homogeneity of the magnetic field related to the RF field, the B_1 field, is an important factor for imaging quality. If a non uniform field is produced by the RF coils the image intensity varies across the image since larger amplitudes of B_1 also cause larger flip angles [48, Chapter 7.4.3]. Inhomogeneities in B_1 not only cause image distortions but also have an impact on many quantification methods like for example the rapid T_1 quantification method used for relaxation phantom evaluation (see Section 2.2.3) [53]. Therefore, also this factor was evaluated for the created phantom with a method based on an effect called Bloch-Siegert shift [54].

Bloch-Siegert B_1^+-Mapping

When an off-resonance RF field is applied the resonance frequency of protons shifts according to the already mentioned effect - the Bloch-Siegert shift. This shift can be applied for the mapping of B_1 field variations when an off-resonance pulse is applied after an excitation pulse. This offresonance pulse's frequency has to be located far enough away from the excitation frequency to avoid further excitation of the spins. According to the Bloch-Siegert shift the frequency of the spins changes during the off-resonant pulse and as a consequence a phase shift proportional to the squared B_1 magnitude can be observed [54].

Image Acquisition

Two 3D GRE records with TR = 102ms, TE = 13.6ms and α = 60° were acquired for the whole phantom volume in 32 slices of 2mm with 128 x 128 voxels each in a FoV of 227 x 227mm. The offresonance RF-pulse was applied between exitation and readout with a duration of 10ms to create the Bloch-Siegert shift. The pulse had an onresonant equivalent flip angle of 1000° for both images with a frequency shift with respect to water of 4 kHz for the first and -4kHz for the second image.

Data Processing

The acquired data was feed into an algorithm for ultrafast 3D Bloch-Siegert B_1^+-Mapping that uses variational modeling [55].
A resulting B_1 map was then used for further evaluation regarding the spatial distribution of B_1 inhomogeneities in the phantom volume.

2.2.3 Measurements regarding Relaxation Times Phantoms

Transversal Relaxation Time Measurements

Spin Echoes

To measure the time constant T_2 a sequence of spin echo (SE) images can be used. The signal that can be recorded with a SE decreases with rising TE according to an exponential function with the time constant T_2 (see Equation 2.14). The reason for the independence of SE from B_0 field inhomogeneities is a π pulse (refocusing pulse) that rephases the spins that where dephased due to B_0 inhomogeneities earlier [48, Chapter 8.2].

$$M(TE) = M_0 e^{-TE/T_2} \tag{2.14}$$

A very important factor to prevent measurement errors is the chosen TR. If TR is chosen too small the longitudinal magnetization $M(t)$ will not fully relax to the equilibrium magnetization M_0 before the next excitation pulse and therefore the measured signal is less than theoretically described in Equation 2.14. Considering the impact of TR on $M(t)$ a modified Equation 2.15 can be stated. If the effect of TR shall be minimized it should be chosen to be five times larger than the longest T_1 in the area in which T_2 should be evaluated [56, Page 150][48, Chapter 8.3].

$$M(TE, TR) = M_0(1 - e^{-TR/T_1})e^{-TE/T_2} \tag{2.15}$$

An other method that may be considered is a multi spin echo where one excitation pulse is followed by a series of refocusing π-pulses, which decreases measuring time noticeably [48, Chapter 8.2]. The drawback of this method is a strong influence of stimulated echoes on the measured signal and therefore it is not of sufficient accuracy for the application at the created phantoms [57].

Longitudinal Relaxation Time Measurements

Inversion Recovery

The gold standard for the measurement of T_1 is a sequence called inversion recovery (IR). In IR at first a π pulse IR the longitudinal magnetization to the negative direction. After a inversion time T_I the remaining longitudinal magnetization is flipped to the transversal plane with a $\frac{\pi}{2}$ pulse and then the signal is measured. When several of these IR images with different inversion times are recorded the time constant T_1 can be evaluated. With the assumption of ideal π and $\frac{\pi}{2}$ pulses in Equation 2.16 the signal progress after a $\frac{\pi}{2}$ pulse can be seen. Since TE is kept constant across the acquisition series e^{-TE/T_2} can be considered as a constant factor. This implies that the only unknown parameter in $M(TI, TE)$ is T_1 [48, Chapter 8]. Since imperfect inversion is a big issue in T_1 quantification as inversion pulse an adiabatic pulse was used, which has a low sensitivity to B_1 inhomogeneities [58].

$$M(TI, TE) = M_0(1 - 2e^{-TI/T_1})e^{-TE/T_2} \tag{2.16}$$

Rapid T_1 quantification

Since IR is very time consuming also faster methods have been developed. The method utilized for this thesis was a variable flip angle method that utilizes a model based reconstruction approach for 3D radially recorded data. The pulse sequence used for that method was RAVE with a golden-angle ordering scheme [53].

Relaxation Times Data Processing

The data processing of the recorded IR and SE images was done for all relaxation times evaluations in the same way. For each pixel a series of intensities can be extracted from the acquired series of images. These intensities can be fitted to their corresponding exponential function (an exponential increase for IR and an exponential decrease for the sequence of SE images). As fitting procedure the "fminsearch" function provided by matlab was utilized. For the SE images the fitted constants can be interpreted as M_0 and

the relaxation time T_2. In IR it is known that a fit of the two parameters M_0 and T_1 is very sensitive to systematic errors as for example non-ideal flip angles due to B_1 inhomogeneity. Therefore, the application of a more robust three parameter fit is suggested [59]. This was achieved by a fit to Equation 2.17 where a describes the coefficient of inversion.

$$M(TI, TE) = M_0(1 - a \cdot e^{-TI/T_1})e^{-TE/T_2} \tag{2.17}$$

Evaluation of Relaxivities

To determine the relaxivities of the used doping agents ($Gd - DO3A - butrol$ and $MnCl_2$) in the created stock solutions (31.26 mM for $MnCl_2$ and 20mM for $Gd - DO3A - butrol$) 4 different concentrations of $MnCl_2$ (varying between 0.02 and 0.6mM) and 5 different concentrations of $Gd - DO3A - butrol$ (varying between 0.07 and 1mM) were filled into vials with 5ml each. The concentrations where chosen in a way that the theoretically resulting relaxation times are in a physiological and therefore frequently measured range. For the 9 vials T_1 and T_2 times were measured with the previously explained methods.
To determine T_1 the IR SE sequence with TE = 11ms, TR = 8000ms and 13 different TI = [40ms, 80ms, 120ms, 160ms, 200ms, 300ms, 400ms, 500ms, 750ms, 1000ms, 1500ms, 2000ms, 3000ms] was used.
For T_2 determination a sequence 13 of SE images with TR = 5000ms and TE = [5ms, 10ms, 15ms, 20ms, 30ms, 40ms, 50ms, 75ms, 100ms, 150ms, 200ms, 300ms, 400ms] were recorded.
For both relaxation time measurements a 2D measurement of a 5mm slice with 128 x 64 voxels in a FoV of 180 x 90mm. The resulting relaxation times and their corresponding concentrations were then fitted to equations 2.1 and 2.2 in order to result in the relaxivities for $Gd - DO3A - butrol$ and $MnCl_2$.

Evaluation of T_1 and T_2 of the Relaxation Phantoms

For T_1 measurements IR and the rapid T_1 quantification method explained in [53] were used, for T_2 the single SE sequence with different TE was used. Both methods were recorded in 2D in a 5mm slice with two different resolutions in two measurement sets. The first set was measured with a

pixel spacing of 1.145mm and the second with 1.445mm in phase encoding as well as in frequency encoding direction. The measurement sets were composed as Set1 = [T1-2, T1-3, T1-4, T1-5, T1-6, T1-7, T1-8, T2-2] and Set2 = [T1-1, T2-1, T2-3, T2-4, T2-5, T2-7, T2-8] (see Phantom Labels in Tables 3.2 and 3.3).
For IR a TE of 11ms was chosen, TR was 10000ms and the acquired images had inversion times TI = [40ms, 80ms, 120ms, 160ms, 200ms, 300ms, 400ms, 500ms, 750ms, 1000ms, 1500ms, 3000ms].
Spin echoes were acquired with a repetition time TR = 10000ms and the echo times for the images were adjusted as follows - TE = [11ms, 15ms, 20ms, 30ms, 40ms, 50ms, 75ms, 100ms, 150ms, 200ms, 300ms, 500ms].
For the rapid T_1 quantification 10 flip angles between 1° and 19° in 2° steps with 89 spokes were acquired in 3D with the RAVE sequence. Here 256 x 256 x 40 voxels in a FoV of 227 x 227 x 2mm were imaged with TR = 5.38ms and TE = 2.46ms. In addition to the RAVE images a 3D B_1-map was necessary and therefore the Bloch-Siegert method mentioned in Section 2.2.2 where all parameters stayed the same.

Evaluation of Temperature Dependence of Relaxation Times Phantoms

Since T_1 of gadolinium and manganese [60] are known to be highly temperature dependent the relaxation time variation due to a variation of temperature was evaluated. In order to avoid a damage of the final T_1/T_2-phantoms (due to expansion and contraction of water with temperature variation) a different set of ten phantoms was used for this experiment. The adjusted relaxation times were T_1 = [200ms, 800ms, 1000ms, 440ms, 800ms, 800ms, 800ms, 800ms, 800ms] and T_2 = [165ms, 165ms, 165ms, 30ms, 90ms, 115ms, 140ms, 190ms, 215ms]
To be able to evaluate the temperature dependence of the phantoms relaxation times were measured for three temperatures T = [20°C, 37°C, 50°C]. In order to keep the phantoms at the designated temperatures they were put into a water bath that was supplied with tempered water by tubes connected to a water pump with heating function. To monitor the temperature inside the water pump as well as in the water bath optical temperature sensors (FOT Lab Kit Fluoroptic Thermometer, Luxtron Corporation) were used.

The preparation for the experiment started with the connection of all required tubes and care had to be taken that the pump is located lower than the jar for the water bath since the water backflow was passive and therefore only effective if no potential has to be overcome. Afterwards the tubes had to be vented and the inflow had to be regulated by squeezing the tube to get a balance between in- and outflow so that the water in the jar neither totally flows off nor an overflow occurs.
As soon as the water bath was located inside the scanner some time was needed until the water temperature inside the water bath equalized. Subsequently the phantoms were allowed to equalize their temperature with the water bath for 45 minutes before the measurements started. During the measuring process one person was inside the scanner room to observe the liquid level in the water bath and thereby prevent a total flow off as well as an overflow.

To acquire knowledge about the relaxation times of the phantoms for each temperature IR T_1 measurements (see Section 2.2.3) with TE = 11ms and TR = 5000ms and TI = [80ms, 120ms, 200ms, 400ms, 500ms, 1000ms, 1500ms] were executed. Additionally a spin echo T_2 measurement (see Section 2.2.3) was carried out with TR = 5000ms and TE = [11ms, 20ms, 40ms, 75ms, 100ms, 150ms, 200ms]. TR for these measurements was chosen to be smaller than for the other measurements to shorten the scan-time though this can lead a systematic measurement error as described in Section 2.2.3.

Evaluation of Long Term Stability

For an insight on the long term stability of the relaxation phantoms the measurements of their relaxation times were repeated exactly three month after the initial evaluation. T_1 and T_2 were measured with IR and a sequence of single SE respectively and the the same parameters as in Section 2.2.3 were used. The pixel spacing was 1.523mm x 1.523mm. Phantom T2-6 was not evaluated for long term stability since it was excluded immediately after the initial relaxation times evaluation due to an imperfect seal. It was decided not to prepare a new phantom since T1-4 basically has the same relaxivity properties anyway.

2.2.4 Measurements regarding Fat-Water Phantoms

Spectroscopy

Magnetic resonance spectroscopy is the gold-standard method in order to quantify the amount of fat and water in substances. Depending on their chemical environment protons are shielded from the surrounding magnetic field. This causes different Larmor frequencies for protons in different locations inside one molecule. This effet is called chemical shift. The spectrum is gained by calculating the Fourier transform of the free induction decay (FID). Different peaks can be seen and they can be referred to chemical surroundings of hydrogen nuclei. Provided that the spectra of fat and water are known they can be separated in a mixed spectrum. The ratio of the areas under the separated peaks correspond to the ratios of fat and water [41, 61].

Data Acquisition

As measurement technique a single voxel spectroscopy sequence called STEAM was used. This sequence consists of three subsequent 90° pulses each encoding one orthogonal direction so only one voxel is stimulated by all pulses and hence the resulting stimulated echo can be considered to originate from one voxel [61]. With STEAM short echo times compared to other spectroscopy sequences can be achieved. This can minimize effects due to varying T_2 in different peaks of the spectra. Measurements regarding the fat-water phantoms were performed with TE = 5.4ms. Preparatory to the measurements the magnetic field inside the chosen voxel had to be manually shimmed to improve the homogeneity and thereby the measurement quality. For each phantom 10 measurements were averaged to increase the signal to noise ratio. A bandwidth of 2000 Hz was chosen for a voxel with size 18mm x 18mm x 20mm. The voxel was placed in the centre of the phantom with a gap to the bottle walls.
For high water concentrations the water peak rises significantly in the spectrum so that the fat peaks become almost invisible. To overcome this issue for water concentrations between $30\%_{vol}$ and $90\%_{vol}$ two spectra were acquired. One as described previously and one with an additional water suppression pulse.

Data Processing

The measured spectra were viewed with jMRUI v5.2 [62, 63]. Also the processing of the spectra were performed with this software. For phase correction the zeroth-order phase error (due to a mismatch between receive and excitation channels [56]) and a timeshift (which causes a phase error of first order) were compensated. Subsequently the peaks of each spectrum were seperated and quantified using the AMARES algorithm [64]. For this analysis the peaks and their full-width-half-maximum had to be selected manually and then Lorentzian lines were fitted to the shape of each peak. The manual selection was done with the knowledge of the ideal shape of a fat spectrum as it can be seen in Figure 2.8. With the fitted Lorentzian lines areas and therefore the signals of fat and water can be calculated. For water concentrations larger than 30%$_{vol}$ only the water peak was fitted in the complete spectrum. All fat peaks were gained from the water suppression spectrum since only there the smaller fat peaks are visible due to a higher signal resolution. In order to get the fat fractions the gathered signal fractions have to be corrected with the proton density correction stated in hereafter.

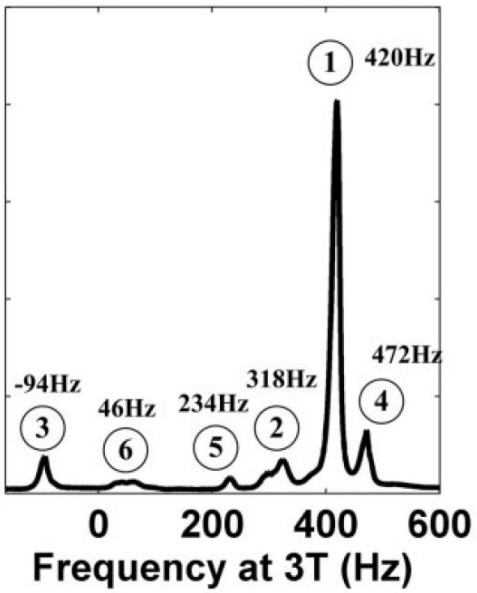

Figure 2.8: Spectrum of peanut oil with all it's relevant peaks which is similar to the spectrum of adipose tissue [43].

IDEAL

IDEAL is the abbreviation for iterative decomposition of water and fat with echo asymmetry and least squares estimation and a high resolution imaging method for fat-fraction quantification. This algorithm is based on a fat water separation method called two-point Dixon method [65]. Two-point Dixon method utilizes the phase-shift between water and fat due to the chemical shift between fat and water. The precession frequency of fat and water protons is different and this leads to an oscillation in the FID. If now two images are recorded at a maximum and at a minimum of the FID they are labeled as in-phase and out-of-phase image. The oscillations are originated from the phase shift between fat and water and therefore with the combination of the two images information about fat and water fractions can be gained. An influencing factor that can decrease the quantification quality substantially is B_0 field inhomogeneity. A variation of the local magnetic field leads to phase shifts that distort the evaluated chemical shift severely. For a removal of B_0 dependencies one additional image acquisition has been added and used for the quantification of B_0 inhomogeneities [66]. With the use of an iterative least squares approach [67], gradient echo imaging [68] and the integration of a multipeak model of fat spectra [43] for quantification of the fat and water fractions an accurate analysis of fat fractions can be assumed as previously investigated [41].

In the presently used modified IDEAL algorithm a multipeak fat model and a sophisticated algorithm - total generalized variation (TGV) - was applied in order to integrate a piecewise smooth constraint on the B_0 field estimation. Hence, the quality of the B_0 estimation as well as of the fat fraction quantification was improved.[19]

Image Acquisition

For the evaluation of the prepared phantoms four 2D GRE images with different TE = [2.25ms, 5.57ms, 8.89ms, 12.20ms], TR = 60ms and α = 30° were acquired. In order to be able to do sufficient analysis the magnitude as well as the phase of the images had to be recorded. The images were aquired in a 3mm slice with 256 x 256 voxels that represent a FoV of 210 x

210mm.

Additionally to the GRE the spectrum of the fat phase was acquired in order to be able to estimate the fat fractions with a multipeak model that represents the chemical structure of the created fat phase. The spectrum was recorded with a PRESS sequence. In contrast to STEAM the PRESS sequence uses 180° pulses which increase the signal amplitude [61]. Since TE cannot be chosen arbitrarily short the T_2 decay until the spectrum was recorded had to be considered. To be able to correct the spectrum with respect to relaxation effects five spectra with different TE = [30ms, 40ms, 50ms, 60ms, 80ms] were recorded.

Data Processing

The four GRE images were used as input for the modified IDEAL analysis. As additional input the spectrum of the fat phase was necessary. To be able to provide a correct distribution of signal on the different peaks in the spectrum each of the five spectra was analysed as described before. With knowledge of the areas of each peak T_2 for each peak in the spectrum was calculated and used for a correction (the peak height at t=0 was calculated). The results of the modified IDEAL analysis were estimations of T_2^*, B_0, a fat image and a water image. In order to result in a fat fraction in $\%_{vol}$ the proton density correction as described below was applied.

Proton Density Correction

Often Equation 2.18 is used as estimation of fat fractions which is probably the most intuitive way of fat signal fraction η calculation with known fat signal S_f and water signal S_w.

$$\eta = \frac{S_f}{S_f + S_w} \tag{2.18}$$

However, this represents the fat signal fraction which differs from the more relevant fat volume and fat mass fractions. The mismatch between those fat fraction measures is due to an influence of mass density and protons per molecule of each phase on the signal fraction. In Equation 2.19 the corrected

Table 2.4: Fat Water Phantom Ingredients and their molecular weights, mass densities and number of protons per molecule [69, 70]

Ingredient	MW in $\frac{g}{mol}$	ρ in $\frac{g}{ml}$	λ unitless
Water	18.015	0.933	2
Agarose	631	0.9	38
Sodium Dodecyl Sulfate	288	1.01	25
Stearic Acid	284	0.94	36
Peanut Oil	879.52	0.893	105.6

fat volume fraction is stated [69]. Here MW is the molecular weight, ρ the mass density and λ the number of protons per molecule each for the fat and water phase. In case of the present phantom things get even more complicated. Since fat and water phase consist of more than one ingredient a mean was used where the weighting factor w is the mass fraction of each ingredient. The values for each ingredient can be seen in Table 2.4 and how the parameters for peanut oil are estimated is stated below. All further added ingredients were omitted in these calculations since they were present in a very small amount compared to the stated components.

$$\eta = \frac{S_f \sum_i w_{f,i} \frac{MW_{f,i}}{\rho_{f,i}\lambda_{f,i}}}{S_f \sum_i w_{f,i} \frac{MW_{f,i}}{\rho_{f,i}\lambda_{f,i}} + S_w \sum_i w_{w,i} \frac{MW_{w,i}}{\rho_{w,i}\lambda_{w,i}}} \tag{2.19}$$

Peanut oil parameters

For the calculations regarding the fat fraction correction the main components of the fatty acid composition of peanut oil have to be known [71]. The fatty acids and their quantities can be seen in Table 2.5. The method for the calculations of the molecular weights was adopted from an online calculator [72] where the molecular weight of single fatty acids calculated with knowledge of the number of carbon atoms and double bonds in the molecules. The total molecular weight is gained as stated in Equation 2.20 where f_i is the weight fraction of a fatty acid and MW_i it's molecular weight. The average molecular weight is multiplied by three since fat is organized in a triglyceride and the added constant is the molecular weight of glycerol.

Table 2.5: Main fatty acids of peanut oil [71]

Fatty acid	Quantity in %
C16:0 (palmitic acid)	7.5
C18:0 (stearic acid)	2.1
C22:0 (behenic acid)	1.01
C18:1cis(n-9) (oleic acid)	71.1
C18:2cis(n-6) (linoleic acid)	18.2

The density was simply calculated as the density's average of the single fatty acids which were gathered from pubchem [70]. In order to know the protons per molecule of peanut oil Equation 2.21 was applied which is similar to the MW calculation. Here the λ_i of each fatty acid was estimated as twice the number of carbons minus the number of double bonds which both can be seen in the notation for the fatty acid. The multiplication with three can be justified as for the MW calculation and the addition with a constant is the amount of protons in glycerol.

$$MW = 3 \cdot \frac{\sum f_i \cdot MW_i}{\sum(f_i)} + 38.049 \tag{2.20}$$

$$\lambda = 3 \cdot \frac{\sum f_i \cdot \lambda_i}{\sum(f_i)} + 5 \tag{2.21}$$

T_1 and T_2 evaluation of Fat- and Water-Phase

To see that the relaxation times of the fat and water phase are in a physiological range T_1 and T_2 were evaluated with IR and a sequence of SE as it is described in Section 2.2.3. For T_1 measurement TE was 11ms, TR 15000m and the 12 recorded echoes had the following inversion times TI = [40ms, 80ms, 120ms, 160ms, 200ms, 300ms, 400ms, 500ms, 740ms, 1000ms, 1500ms, 3000ms]. Regarding the T_2 measurement TR was 10000ms and the 12 images were recorded with TE = [11ms, 15ms, 20ms, 30ms, 40ms, 50ms, 75ms, 100ms, 150ms, 200ms, 300ms, 500ms]. The data was recorded in 2D with a slice thickness of 5mm and the pixel spacing was 1.047 x 1.047mm.

Evaluation of Long Term Stability

The fat fractions measured with the modified IDEAL method was repeated approximately four month after the final evaluation in order to get an insight on the long term stability of the created phantoms. The measurement procedure was the same as described above.

2.2.5 Measurements regarding Magnetization Transfer Phantoms

Quantification of MT Effects

The phenomenon of MT can be modelled as a two-pool model. It is assumed that there is a bound pool where protons are bound in macromolecules and a free- or liquid pool in which protons are in bound small molecules. The magnetizations of both pools (M_f is the magnetization of the liquid pool and M_b the magnetization of the bound pool) are coupled with each other by the transfer rates k_r from the free to the bound pool and k_f vice versa. Equations 2.22 and 2.23 show the basic two pool model. If the constants in the model are fitted the ratio of bound pool to free pool (f) can be calculated as stated in Equation 2.24. This ratio is related to the bound pool fraction (BPF) which can be calculated as f/(f+1) [45, 47].

$$\frac{dM_f(t)}{dt} = -M_f(t)(R_{1,f} + k_r) + M_b(t)k_f \tag{2.22}$$

$$\frac{dM_b(t)}{dt} = -M_b(t)(R_{1,b} + k_f) + M_f(t)k_r \tag{2.23}$$

$$f = \frac{k_f}{k_r} \tag{2.24}$$

A more straight forward way to get an insight on the amount of MT effect in an object is the calculation of the magnetization transfer ratio (MTR). MTR describes the amount of MT that can be observed in a tissue and it can be calculated as stated in Equation 2.25. Here M_{SAT} is the reduced signal that

can be recorded if an saturating RF-pulse is sent before image acquisition and M_0 is the unperturbed signal [45].

$$MTR = \frac{M_0 - M_{SAT}}{M_0} \tag{2.25}$$

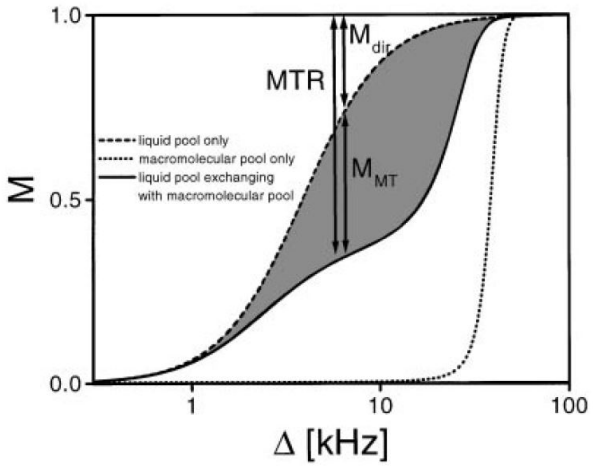

Figure 2.9: Illustration of an example for magnetization differences between liquid and macromolecular pools in dependence of the offset frequency of a saturation pulse [45].

Initial MTR Experiments

Before the MT phantoms were prepared the needed amount of ovalbumin to create a physiologically relevant MT effect had to be figured out. For this first evaluation the MTR was chosen for comparisons with tissue. Therefore, three dilutions with different concentrations (10%$_{mass}$, 20%$_{mass}$ and 33%$_{mass}$) of ovalbumin were produced. Higher ovalbumin concentrations were not investigated since it was not possible to dissolve more ovalbumin in water. The protein was slowly diluted in water and after a night of storage (to prevent dissoved air bubbles inside the measurement areas) crosslinking was performed with heating the probes in a water bath at 85°C for 10 minutes.

For determination of the MTR two 2D GRE images were recorded. Both with TE = 2.25ms, TR = 60ms and α = 30°. One of the images was recorded with

an additional magnetization transfer saturation pulse make the MT effect visible (resulting in an image that visualizes M_{SAT}). The slice thickness was 3mm and the pixel spacing 0.781 x 0.781mm.

The MTR was calculated by averaging the signals in a homogeneous region inside the test vials and applying Equation 2.25 on the average intensities.

T_1 and T_2 Measurements of raw Ovalbumin Dilution

To calculate the necessary amounts of doping agents the relaxation times of the chosen ovalbumin concentration ($33\%_{mass}$) was determined with the spin echo method and inversion recovery.
For inversion recovery TE = 11ms and TR = 15000ms were chosen. Six images with inversion times TI = [120ms, 300ms, 500ms, 750ms, 1500ms, 3000ms] were recorded. The smaller inversion times were skipped for this measurement since a T_1 significantly smaller than 1000ms was not expected.
To determine T_2 six spin echoes with TR = 10000 and TE = [20ms, 75ms, 150ms, 200ms, 300ms, 500ms] were acquired. Also here some of the shorter echo times were skipped since no short T_2 was expected.
For all measurements 2D images were acquired with a slice thickness of 5mm and 0.703 x 0.703mm pixel spacing.

Quantitative Magnetization Transfer Measurements

For evaluation of the final MT phantoms, MT parameters were evaluated quantitatively by using a large set of different magnetization transfer off-resonance saturation pulses. The further the frequency of the saturation pulse is shifted from resonance the less the signal amplitude is influenced by the saturation. This dependence between signal and frequency shift is called z-spectrum and can be determined for all created magnetization transfer phantoms by fitting the acquired data to a magnetization transfer model. As prior knowledge T_1, T_2, a B_1 map and a B_0 map were acquired.

Magnetization Transfer Image Acquisition

The data for modelling the MT effects in the created phantoms consists of 40 records. These GRE images were recorded with offresonance RF-pulses which vary in their amplitude as well as in their frequency shift. The different amplitudes are given as onresonant equivalent flip angle α = [600°,800°,1000°]. Recorded off-resonance frequencies were [300Hz, 500Hz, 800Hz, 1kHz, 2kHz, 3kHz, 4kHz, 5kHz, 6kHz, 7kHz, 8kHz, 9kHz, 10kHz]. As a reference additionally one GRE image without any saturation pulse was acquired. TR for these images was 121.1ms. The saturation pulse had a duration of 19ms, the excitation pulse of 2ms. Between the offresonance pulse and the excitation pulse a delay of 2.1ms was used, between the excitation pulse and the next magnetization transfer saturation pulse 98ms passed.

Prior Knowledge Procurement

To gain prior knowledge regarding T_1 and T_2 the same techniques as described in Section 2.2.3 were used. For all measurements TR was 10000ms. A TE of 11ms was used for T_1 measurements. Inversion times were set to TI = [40ms, 80ms, 120ms, 160ms, 200ms, 300ms, 400ms, 500ms, 750ms, 1000ms, 1500ms, 3000ms]. T_2 was acquired with a variation of TE = [11ms, 15ms, 20ms, 30ms, 40ms, 50ms, 75ms, 100ms, 150ms, 200ms, 300ms, 500ms]
In order to get a B_0-map the the IDEAL B_0-estimation mentioned in Section 2.2.1 was applied with all MT phantoms placed in the phantom housing and embedded in water. TE for the four acquired gradient echo images was [2.25ms, 5.57ms, 8.89ms, 12.20ms].
A B_1-map was acquired as described in Section 2.2.2.

Data Processing

As data processing tool qMRLab [73], with the method *"qmt_spgr"* was used. This method evaluates quantitative Magnetization Transfer (qMT) using Spoiled Gradient Echo (or FLASH). It can simply be fed with maps of all prior knowledge as well as with a 3D-matrix containing all images saturated with different offresonance pulses. Solely T_2 has to be set for each MT phantom separately and therefore each phantom had to be fitted on it's

own. As model for the fitting routine a two-pool model based on the work of Yarnykh was used [74].

Long Term Stability

Since the MT phantom was created in order to verify relaxation measurements the relaxation time evaluations of the created phantoms were repeated after exactly three month. This measurement was performed together with the long term stability evaluation of the relaxation phantoms. Therefore the measurement parameters can be seen in Section 2.2.3.

3 Results

3.1 B_0 Homogeneity

3.1.1 Glass Bottle Evaluation

For each direction and combination of bottles a B_0-map was acquired to investigate the homogeneity (see Figure 3.1). In each bottle there are brighter regions at the bottom and also near the bottleneck which implies more inhomogeneities. Even though the area between these brighter regions seems to be homogeneous.

A better insight to the differences in the configurations is given in the following boxplot (see Figure 3.2). It can be seen that the interquartile range for all configurations is of comparable size (less than 25Hz for all configurations) as well as the median. The only configuration that differs noticeably is the sagittally imaged bottle which has a lower median and more outliers than the other configurations.

Four different B_0 field profiles for a single bottle embedded in air were extracted and can be seen in Figure 3.3. The blue line in this figure is in the same region as the region selected for the boxplot (see Figure 3.2) and it can be seen that the other field profiles have a much higher variation of B_0.

Regarding the T_2^* evaluation the largest possible T_2^* in the region that can be seen in Figure 3.4 with a B_0 influence less than 10% was 20ms. This was as all previous measurements evaluated for a bottle surrounded with air. To see if the influence can be decreased with an other surrounding medium the bottle was embedded in water and the measurements were repeated. With water as embedding medium a T_2^* up to 47ms can be evaluated with a T_2^* distortion of less than 10% due to B_0 inhomogeneities.

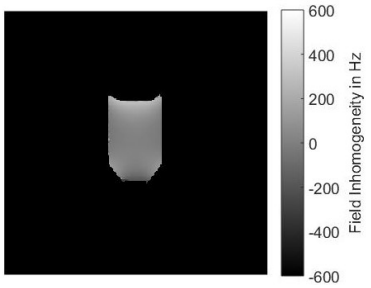

a: single bottle imaged in the coronal plane

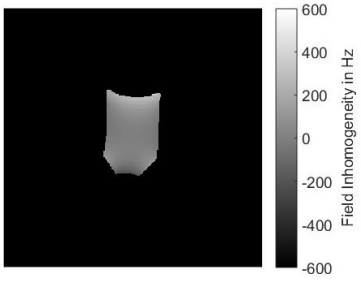

b: single bottle imaged in the sagittal plane

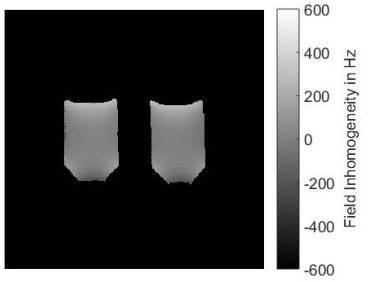

c: two bottles aligned horizontally next to each other

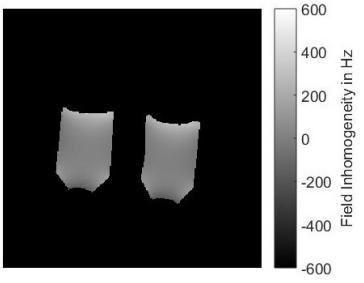

d: two bottles stacked vertically above each other

Figure 3.1: Overview of homogeneity variation in different bottle configurations

3.1.2 Housing Evaluation

To visualize the B_0 field inhomogeneities inside the housing a B_0 field map in a coronal and transversal cut is shown in Figure 3.5. It can be seen that the border bottles are slightly influenced from the susceptibility jump from air outside the housing to the water inside the housing whereas the centered bottle is located in a relatively homogeneous field. Field profiles were evaluated for the centered bottle and as example for one of the surrounding bottles. The field profiles were located again as shown in Figure 3.3. The resulting field profiles can be seen in Figure 3.6 and there a difference in homogeneity between the middle bottle and the border bottle can be observed. Furthermore, the field profiles are more homogeneous than for the evaluation in air (compare Figures 3.3 and 3.6) whereas the field variation in B_0 direction is larger.

For the T_2^* evaluation in the housing the most homogeneous slice was used as region of interest in the centre of the middle bottle as well as in the centre

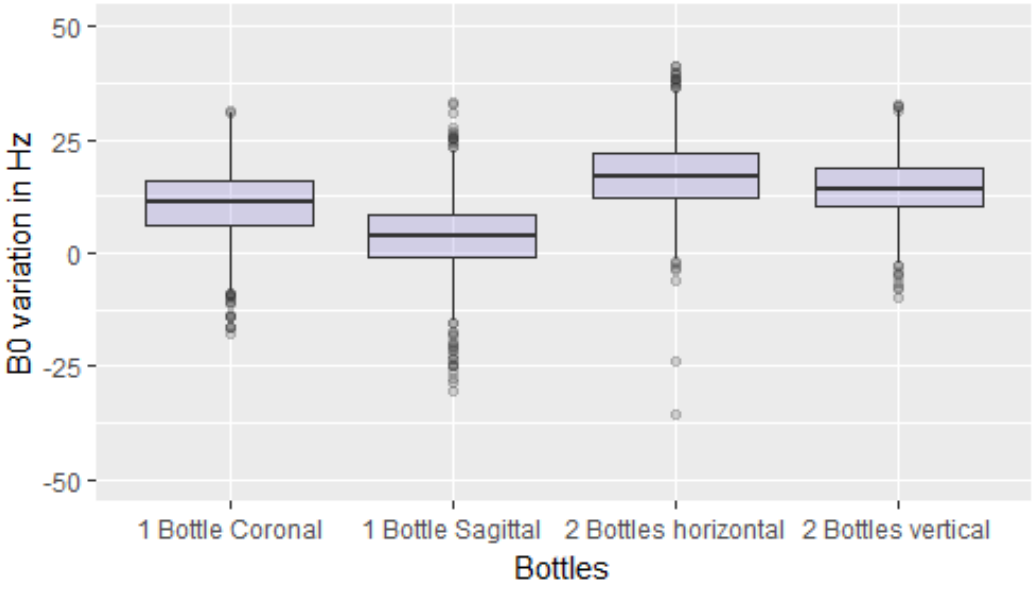

Figure 3.2: Boxplot of the B_0 variation within the region selected as in Figure 2.7 for four different bottle configurations. The median can be seen as horizonal line in each of the boxes which represent the interquartile range. Outliers are represented as small circles.

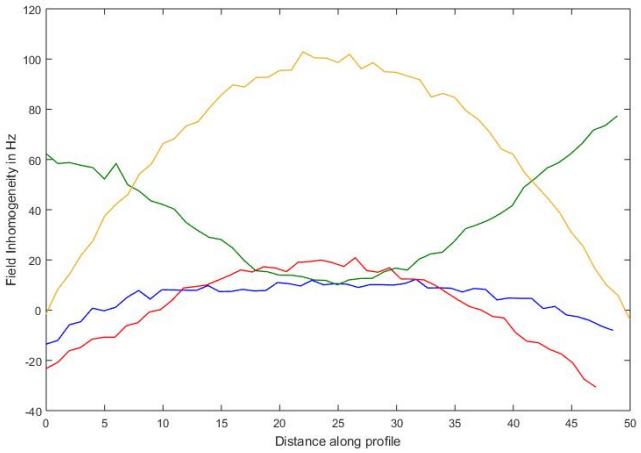

a: Field profiles

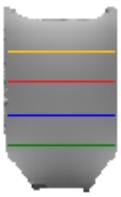

b: Profile locations

Figure 3.3: Four different field profiles as sketched in b) for the single bottle imaged coronally outside the phantom housing

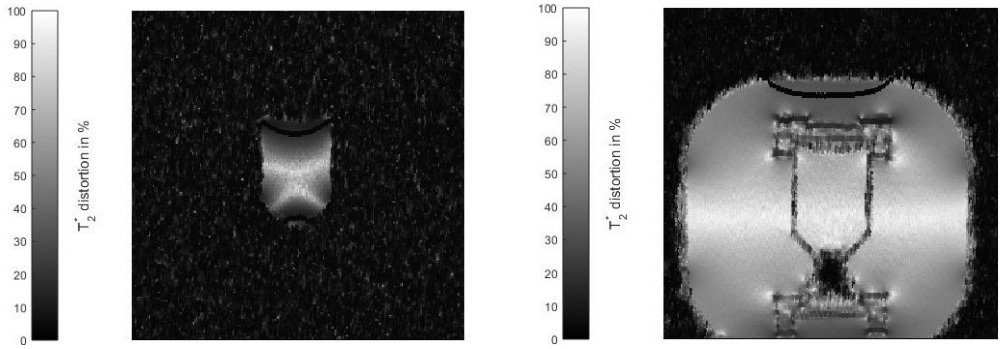

a: Embedded in air

b: Embedded in water

Figure 3.4: T_2^* influence evaluation in bottles embedded in air and water. Field inhomogeneities were applied on a T_2^* of 100 ms according to Equation 2.10

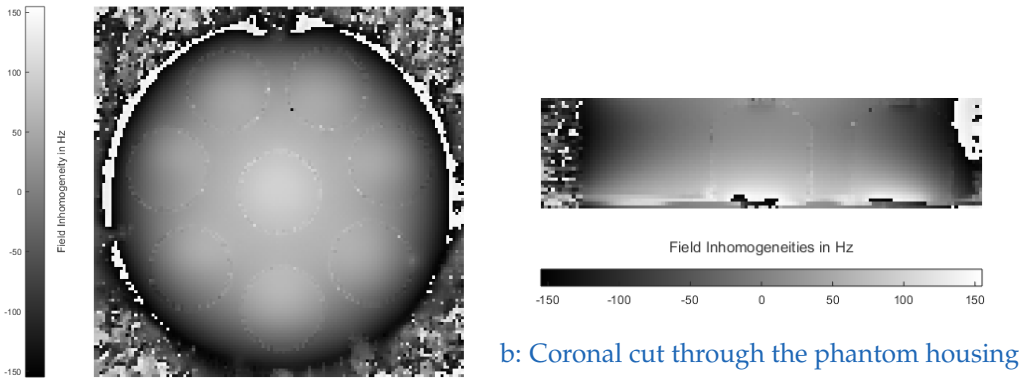

a: Transversal cut through the phantom housing

b: Coronal cut through the phantom housing

Figure 3.5: B_0 field maps inside the phantom housing

of one bottle at the border of the housing. Here a maximum T_2^* of 38.9ms for the middle bottle and values around 20ms for the border bottles are calculated.

3.2 B_1 Homogeneity

To get an overview of the B_1 variation across the phantom housing, B_1 field maps are shown in Figure 3.7 in a coronal and a transversal cut. It can be

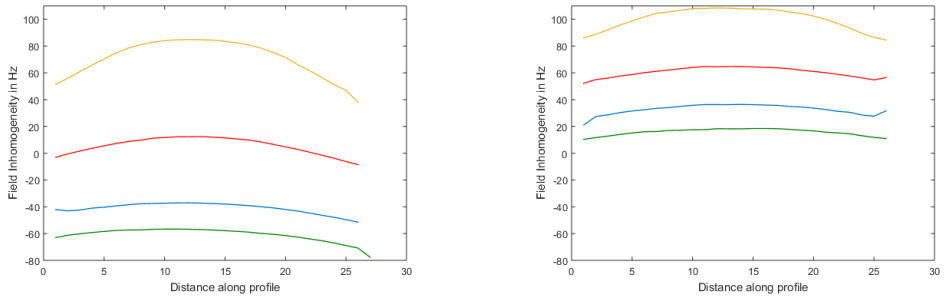

a: Border Bottle

b: Middle Bottle

Figure 3.6: B_0 field variation in bottles inside housing, the slices were selected as in Figure 3.3,b)

seen that inside the bottles at least in the transversal cut the B_1 field can be considered as homogeneous. Outside the bottles fluctuations of the B_1 field can be seen. The flip angles depending on the B_1 variation inside the housing were evaluated for the centred bottle and one surrounding bottle. Field profiles resulting from that evaluation can be observed in Figure 3.8. It can be seen that the resulting field profiles for the border bottle are closer to each other than for the middle bottle and the 100% of nominal flip angle (which implies homogeneous B_1) can be observed for different slices (green and blue) than for the middle bottle (red).

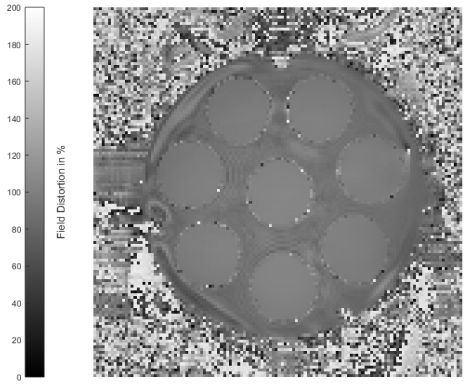

a: Transversal cut through the phantom housing

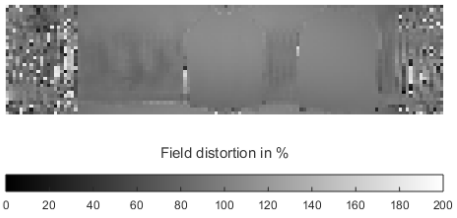

b: Coronal cut through the phantom housing

Figure 3.7: B_1 field maps inside the phantom housing

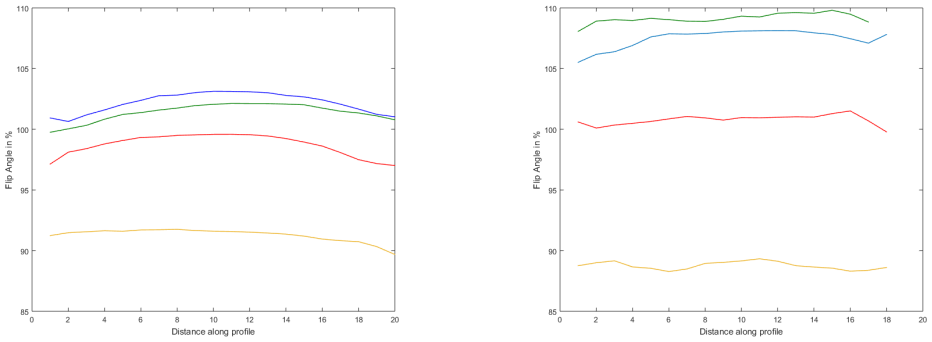

a: Border Bottle b: Middle Bottle

Figure 3.8: B_1 field variation in bottles inside housing, the slices were selected as in Figure 3.3,b)

3.3 Relaxivity Evaluation of Doping Agents

The relaxation times of the doping agents utilized for the created phantoms are plotted in Figure 3.9 with the corresponding fitted linear dependence between doping agent concentration and relaxation times. The resulting relaxivities can be seen in Table 3.1. Here it can be seen that $MnCl_2$ has a distinctly higher influence on T_2 than on T_1.

Table 3.1: Relaxivities of doping agents

Doping agent	r_1 in $\frac{l}{mmol \cdot s}$	r_2 in $\frac{l}{mmol \cdot s}$
$Gd-DO3A-butrol$	4.8592	4.9603
$MnCl_2$	5.4016	91.6095

3.4 Relaxation Phantoms

Two sets of relaxation phantoms were created without any trapped air inside the glass bottles. Their values vary in T_1 while T_2 is fixed and vice versa. Their relaxation times overall only vary slightly from the adjusted values except from some outliers.

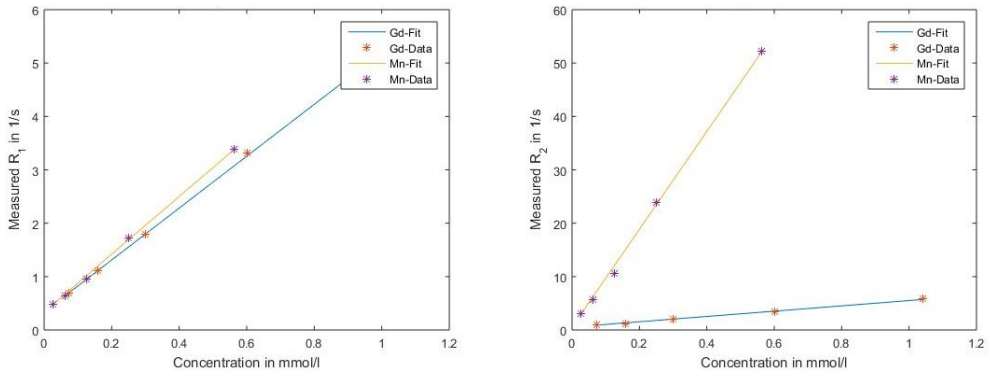

a: r_1 fitting

b: r_2 fitting

Figure 3.9: Relaxivity evaluation of created doping agent stocks.

3.4.1 T_1 and T_2 measurement with gold-standard methods

As reference values T_1 and T_2 were measured with their gold-standard methods which are IR and a sequence of SE with varying TE.
The time constants and their standard deviations σ inside the evaluated regions of interes for all created relaxation phantoms compared to their designated T_1 and T_2 can be observed in Tables 3.2 and 3.3. Phantoms T1-3, T2-7 and T2-8 have slightly larger distinction from their desired values than the other phantoms.

Table 3.2: Relaxation Times for T_1 Phantoms in ms

Phantom Label	T1-1	T1-2	T1-3	T1-4	T1-5	T1-6	T1-7	T1-8
Desired T_1	200	400	600	800	1000	1200	1400	1600
IR - T_1	163	361	322	737	979	1238	1386	1581
IR - σ	0.97	5.17	6.91	5.06	8.53	6.73	8.55	11.81
IR - T_1 aft. 3 m.	156	349	338	735	919	1269	1398	1682
IR - σ aft. 3 m.	1.11	1.60	0.96	2.95	4.85	8.14	7.49	7.84
Desired T_2	165	165	165	165	165	165	165	165
SE - T_2	134	169	109	177	178	182	164	192
SE - σ	3.32	3.25	3.08	3.26	3.51	4.91	3.36	4.83
SE - T_2 aft. 3 m.	133	185	111	169	167	192	161	214
SE - σ aft. 3 m.	2.24	1.42	3.72	1.01	2.49	2.45	0.96	3.80

Table 3.3: Relaxation Times for T_2 Phantoms in ms

Phantom Label	T2-1	T2-2	T2-3	T2-4	T2-5	T2-6	T2-7	T2-8
Desired T_1	440	800	800	800	800	800	800	800
IR - T_1	405	766	709	705	713	768	670	687
IR - σ	2.16	5.56	4.42	1.69	4.58	5.67	2.47	3.51
IR - T_1 aft. 3 m.	467	747	703	689	724	-	679	692
IR - σ aft. 3 m.	1.49	2.31	3.28	3.9	3.11	-	3.19	4.37
Desired T_2	30	65	90	115	140	165	190	215
SE - T_2	28	63	82	106	134	177	175	209
SE - σ	0.25	1.79	1.02	1.74	4.99	4.53	4.84	7.11
SE - T_2 aft. 3 m.	32	60	82	115	135	-	173	199
SE - σ aft. 3 m.	0.58	0.46	0.46	2.61	2.59	-	1.11	1.56

3.4.2 Rapid T_1 quantification

With the rapid T_1 quantification method a mixed set of seven T_1 and one T_2 phantom was scanned. The resulting T_1 values compared to the ones measured with IR can be seen in Figure 3.10. Here a general overestimation of the T_1 values with the rapid measurement method can be observed. Additionally the two phantoms (T2-6 and T2-2) that have the same T_1 measured with the gold standard method result in different T_1 when measured with the rapid T_1 quantification method.

3.4.3 T_1 and T_2 Dependence on Temperature

The rise of relaxation times with increasing temperature can be observed in Figure 3.11. It can be observed that the dependence between temperature and relaxation time has a positive coefficient in general, but does not behave equally for all phantoms.

For the temperature dependence Equations 3.1 and 3.2 can be stated to correct T_1 for a given temperature Θ where $T_{1,23C}$ and $T_{2,23C}$ are reference relaxation times at 23°C, θ_1 and θ_2 are a temperature coefficient that describes the temperature dependence for T_1 and T_2 respectively.

$$T_1(\Theta) = T_{1,23°C}(1 + \theta_1(\Theta - 23°C)) \tag{3.1}$$

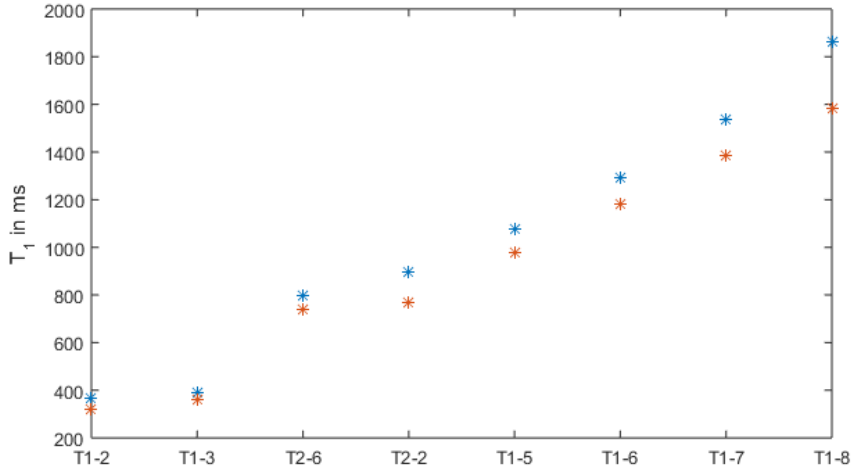

Figure 3.10: Rapid T_1 measurement compared to the inversion recovery method

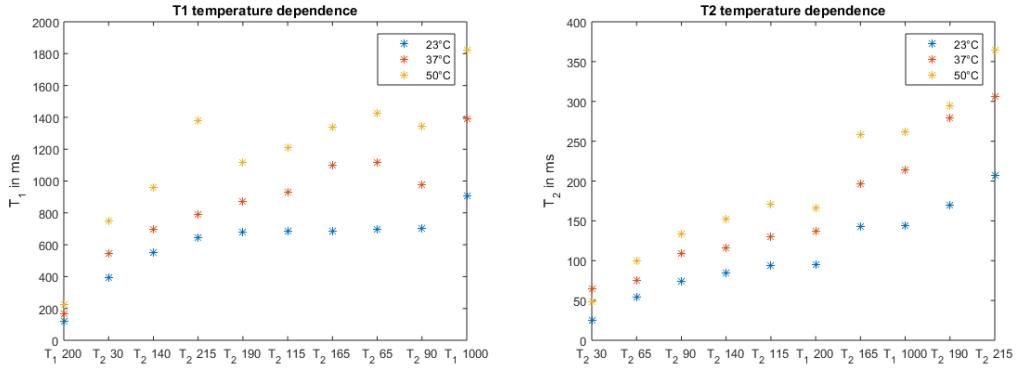

a: T_1 variation for all temperatures

b: T_2 variation for all temperatures

Figure 3.11: Relaxation times for different temperatures

$$T_2(\Theta) = T_{2,23^\circ C}(1 + \theta_2(\Theta - 23^\circ C)) \tag{3.2}$$

For each evaluated phantom θ_1 and θ_2 were computed and plotted in dependence of T_1 and T_2 as it can be seen in Figure 3.12.

According to the quasi linear increase of temperature coefficients with rising relaxation times ($R^2_{T_1}$ = 0.804, $R^2_{T_2}$ = 0.986, for a linear regression with the matlab function "fitlm") θ_1 and θ_2 can be computed with Equations 3.3 and 3.4.

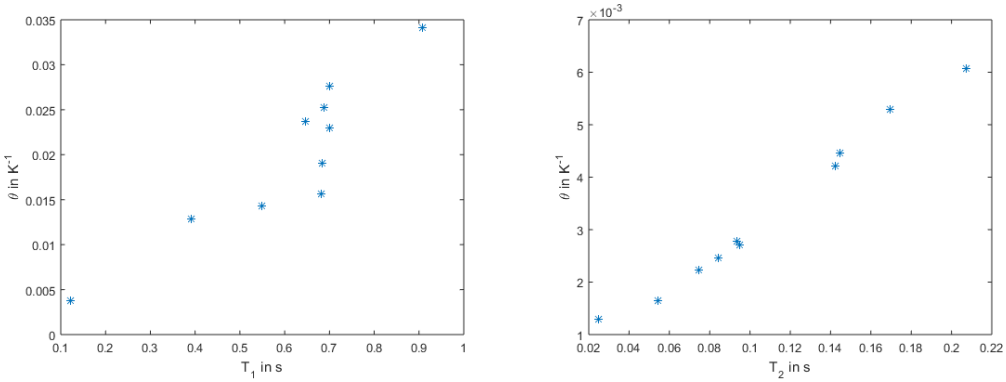

a: T_1 dependence on temperature for all investigated phantoms

b: T_2 dependence on temperature for all investigated phantoms

Figure 3.12: Variation of temperature coefficient θ with relaxation time constants

$$\theta_1 = -0.0024 + 0.0367 \cdot T_{1,23°C} \tag{3.3}$$

$$\theta_2 = 2.1419 \cdot 10^{-4} + 0.0284 \cdot T_{2,23°C} \tag{3.4}$$

3.4.4 Long Term Stability

If the differences between the inital measurements and the measurements after three month are compared (see Tables 3.2 and 3.3) there can be seen that for some phantoms relaxation times varied by less than 10ms (T1-4,T2-2,T2-5,T2-7). Other phantoms had T_1 variations in the range of 100ms (T1-8).

3.5 Fat-Water Phantoms

The created fat-water phantoms' fat fractions differ slightly from the desired values because of inaccuracies while weighting the different phases. However real weights were noted and the resulting fat fractions can be observed in Table 3.4. A noticeable difference can be observed for a desired fat fraction of 80%$_{vol}$ where all measurement techniques result in a fat fraction more than 3%$_{vol}$ higher than the weighted fraction. Further for the weighted fat

fraction of 10.02%$_{vol}$ the spectroscopy method results in a fat fraction of 6.39%$_{vol}$.
For fat fractions larger or equal to 30%$_{vol}$ IDEAL estimates a smaller fat fraction than the spectroscopy method except for 70%$_{vol}$. For smaller fat fractions IDEAL results in higher fat fractions than the spectroscopy method. Further noticeably is that 80%$_{vol}$ is the only fat fraction where the weighted fraction is smaller than both of the measurements.

Table 3.4: Fat Fractions in %$_{vol}$

Desired	Weighted	IDEAL	σ	IDEAL aft. 4 m.	σ aft. 4 m.	Spectro
0	0	0.78	0.93	0.55	0.58	0
10	10.02	9.01	2.01	9.41	1.81	6.39
20	21.05	19.15	1.68	20.51	1.22	18.61
30	29.77	27.55	1.14	27.87	2.63	28.6
40	39.72	37.4	1.27	39.44	1.52	42.68
50	49.63	47.02	1.71	48.85	1.51	51.02
60	60.24	61.17	0.73	63.95	0.96	62.2
70	70.20	71.20	4.07	74.52	4.22	67.81
80	80.06	83.38	2.91	85.54	2.91	84.43
90	95.89	94.68	1.14	94.74	1.81	95.54
100	100	96.51	0.67	98.75	1.04	100

3.5.1 Emulsion Stability and Homogeneity

The first experiments regarding the emulsion creation were done nine month before the finalization of the phantoms. During that time no changes in the emulsions could be observed. Therefore they are considered as stable. The homogeneous distribution of fat and water can be observed in Figure 3.13 where the computed fat fractions are visualized in a coronal cut through the created phantoms.

3.5.2 T_1 and T_2 Measurement of pure Water- and Fat-Phase

The evaluated relaxation times for the water phase are T_1 = 996ms and T_2 = 60ms. For the fat phase a T_1 of 277ms and a T_2 of 50ms were measured.

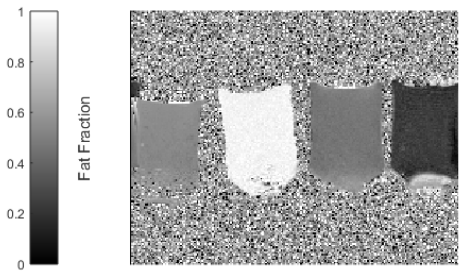

a: From left to right fat the following fat fractions can be seen: 0.5, 0.9, 0.4, 0.2

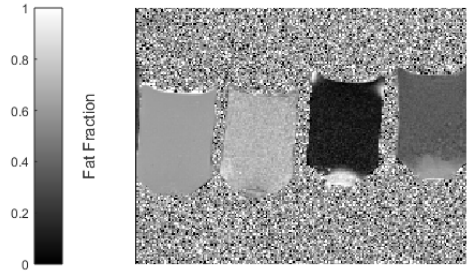

b: From left to right fat the following fat fractions can be seen: 0.6, 0.7, 0.1, 0.3

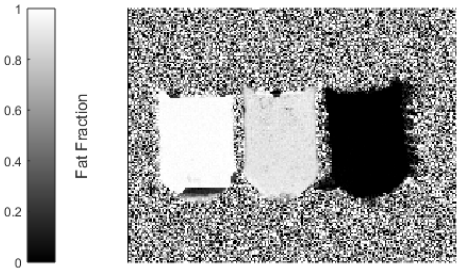

c: From left to right the following fat fractions can be seen: 1.0, 0.8, 0.0

Figure 3.13: Fat-Water Phantoms' estimated fat fractions in coronal cut to see homogeneity

3.5.3 Long Term Stability

The estimated fat fractions of the initial IDEAL measurement and the IDEAL measurement after 4 month (see Table 3.4) correspond very well to each other for small fat fractions. With rising fat fraction the difference between the two measurements increases.

3.5.4 Magnetization Transfer Phantoms

Initial Experiments for determination of appropriate amount of Ovalbumin

The MTR resulting from different ovalbumin concentrations can be observed in Table 3.5. As expected a higher ovalbumin concentration leads to a higher MTR. $33\%_{mass}$ ovalbumin were chosen for the phantom preparation since th corresponding MTR of 0.288 is the closest to a physiological range [26, 75].

Table 3.5: Ovalbumin concentrations for initial experiments in % of mass compared to MTR

Ovalbumin ratio	10%	20%	33%
MTR	0.130	0.173	0.288

T_1 and T_2 of raw Ovalbumin Dilution

For the raw ovalbumin dilution a T_1 of 1054 ms and a T_2 of 44 ms were measured with inversion recovery and multiple spin echoes.

T_1 and T_2 Measurements of Magnetization Transfer Phantoms

The relaxation time measurements for the created MT phantoms resulted in Table 3.6. In general all relaxation times are noticeably smaller than the desired values and the rapid T_1 measurements overestimate the measured T_1 values.

Quantitative Magnetization Transfer Measurements

The quantification of MT parameters in the created phantoms can be observed in Table 3.7. f is the ratio of restricted to free pool, kr the exchange rate from free to restricted pool and kf the exchange rate from restricted to free pool. There can be seen a large variation in all parameters if the phantoms are compared to each other. When Figure 3.14 is considered it can be observed that a higher f leads to a larger measurement error with the

Table 3.6: Relaxation Times for MT-Phantoms

Phantom Label	MT-1	MT-2	MT-3	MT-4	MT-5	MT-6	MT-7	MT-8
Desired T_1	350	500	650	800	920	200	200	200
IR - T_1	264	302	408	555	684	110	120	122
IR - σ	3.89	4.72	22.39	13.19	11.99	5.78	2.31	4.21
IR - T_1 aft. 3 m.	236	270	392	564	718	106	116	111
IR - σ aft. 3 m.	3.23	3.07	15.31	28.8	52.5	0.84	1.48	1.83
Rapid - T_1	305	358	421	648	735	184	155	152
Rapid - σ	3.15	3.26	9.56	2.07	23.97	3.59	4.95	2.89
Desired T_2	40	40	40	40	40	35	30	20
SE - T_2	29	30	35	31	38	21	22	19
SE - σ	0.58	1.05	6.28	0.62	0.96	1.05	0.77	0.99
SE - T_2 aft. 3 m.	24	32	32	35	53	19	21	17
SE - σ aft. 3 m.	1.29	1.48	4.73	8.08	17.76	0.85	0.99	0.61

used rapid T_1 quantification method. A linear regression (with the matlab function ”fitlm”) to this figure leads to an R^2 value of 0.747.

Table 3.7: qMT in created Phantoms

Phantom	f	kr	kf
MT-1	0.0927	14.429	1.0938
MT-2	0.0569	20.816	1.0432
MT-3	0.0388	21.415	0.9043
MT-4	0.0514	39.397	1.9142
MT-5	0.0337	35.800	1.2330
MT-6	0.1330	7.209	0.9435
MT-7	0.0956	4.376	0.4569
MT-8	0.0791	6.687	0.4707

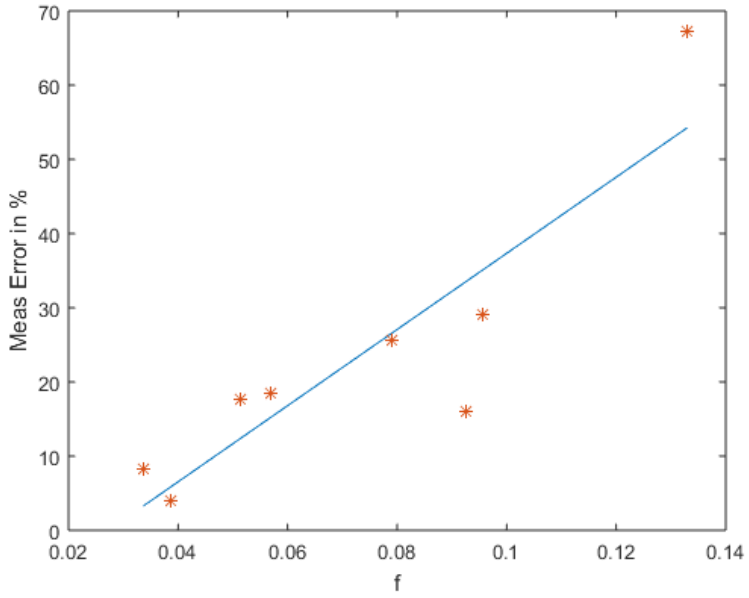

Figure 3.14: Relation of f and the T_1 underestimation with the rapid T_1 quantification

Long Term Stability

A relaxation time measurement after 3 month showed that only slight variations in T_1 as well as T_2 occured. Especially T_2 only differed by less than 5ms for most of the phantoms. Only at phantom MT-5 a distinct increase of both relaxation times can be seen.

4 Discussion

4.1 B_0 Homogeneity

With the investigated results regarding the influence of the different bottle configurations to each other (see Figure 3.2) the placement of the bottles inside the constructed phantom housing can be considered not to influence measurements. Further the homogeneity is improved by the addition of water as embedding media in the phantom as it can be seen in Figure 3.4.

Even though as it can be seen in Figure 3.5 in the presently created phantom housing only the middle bottle can be considered to be in a homogeneous B_0 field. A further improvement on the housing with respect to B_0 field homogeneity might be to increase the length of the acrylic tube [8, Page 77] and place the bottles in the center of this cylinder. This could minimize the variation of magnetic field strength in the B_0 field direction

To be able to image the created phantoms in the present housing with the best possible B_0 characteristics it is recommended to chose a slice that is at the location of the blue line in Figure 3.3.

For measurements that require low inhomogeneity it is further recommended to use the centre bottle space exclusively. To point out the importance of this recommendation it can be referred to the evaluation of influence on T_2^* measurements (see Section 3.1.2). It is shown that in the centered bottles T_2^* that are almost twice as high as for the border bottles can be evaluated with less than 10% distortion.

4.2 B_1 Homogeneity

Figure 3.8 shows the variation of the B_1 distortion. Since the location closest to 100% differs for the center and border bottle a general recommendation on the slice location is difficult. Further the most homogeneous B_1 field for the center bottle is on a different location than the most homogeneous B_0 field (red line for B_1 and blue line for B_0 - compare with Figure 3.3). Since for the border bottles the blue line is close to 100% a possible trade-off between both homogeneity considerations would be to only use the border bottles and image a slice close to the blue line. For measurements where the B_0 homogeneity is of higher importance the center bottle could be used with a slice location between the blue and the red line. To minimize B_1 influence when measuring in the most homogeneous region with respect to B_0 a further possibility is to apply a spatially variant correction factor. A B_1 correction method was applied in the used rapid T_1 quantification method [53] as well. Further it is known that B_1 is dependent on electric conductivity [35] and therefore an improvement of B_1 homogeneity with the addition of $NaCl$ to the water that is filled into the phantom housing may be possible.

4.3 Relaxation Time Phantoms

In general the adjusted and measured (with gold standard methods) relaxation times correspond well to each other. The measured differences to their adjusted values in some phantoms (T1-3, T2-7 and T2-8) may be due to mistakes when pipetting doping agents to the water. Especially when only small amounts of phantom substances were created (for topping up) there can arise mistakes easily.

When the gold standard method is compared to the rapid T_1 measurement besides from a general overestimation of T_1 a hint on a coherence between T_1 estimation accuracy and T_2 could be seen if data points T1-4 and T2-2 are compared in Figure 3.10. These data points have the same T_1 but different T_2 values (165ms and 65ms). For certainty about this coherence further investigations have to be made.

The clear increase of T_1 as well as T_2 with a temperature rise as it can be seen in Figure3.11 has been earlier observed [60, 76]. Also the temperature coefficients that result from Equations 3.3 and 3.4 are in a range that is comparable to the values found in literature [8, Page 56]

Unfortunately after 3 month again air bubbles appeared in the created T_1 and T_2 phantoms. Since no leaky spots could be seen in the bottle necks (as they often did in early experiments) it is assumed that they are rather due to an incomplete degassification than due to bad seals. Even though a repetition of the creation of relaxation phantoms can be suggested if the air bubbles are disturbing any future measurements.

Besides from the arising air bubbles the relaxation times of the phantoms can be considered as stable. For doped agarose gels long term stability observations on relaxation times over one year can be found in literature and the relaxation times stayed constant [77]. Even though some variations in relaxation times regarding their long term stability can be seen in in Tables 3.2 and 3.3. These variations may be due to a sedimentation of doping agents after a long period without any movement. If then the phantom liquid is not mixed sufficiently before a new measurement the relaxation times may be raised. Also the influence of the arised air bubbles could be a conceivable reason for changes in relaxation times. To be sure about this concern on the repeatability of relaxation time measurements with the created phantoms further relaxation time evaluations are necessary. Three month are a very short time period for long term evaluations and future evaluations can be suggested for more informative results. As part of this work no further long term stability measurements could be taken for temporal reasons.

4.4 Fat-Water Phantoms

For the fat-water phantoms stable emulsions were created over the full range of fat fractions that have relaxation times for the water phase that are in a physiologically relevant range. If compared with the relaxation times of tissue in Table 2.1 T_1 is comparable with a T_1 of white matter, or the spinal cord and slightly higher than the T_1 of liver tissue and T_2 lies in the range

of liver tissue as well as heart muscle and cartilage tissue.

For the measurement of the desired $10\%_{vol}$ of fat probably the spectroscopy method underestimates the real fat fraction since the water peak in this spectrum is so large that a bad water suppression could lead to fat peaks that cannot be quantified correctly (especially the fat peaks close to the water peak). The general high measured value of fat fraction if compared to the weighted value for $80\%_{vol}$ can be explained by an observation during the preparation of this phantom. Here a small amount of the water phase settled at the bottom of the bottle and therefore in the rest of the phantom the fat fraction rose. For high fat fractions the fat content is underestimated by the IDEAL measurement. This could be caused by prior assumptions of the used IDEAL algorithm which expects the presence of water in the signal.

There were no macroscopically visible changes in the emulsions after 4 month. The IDEAL measurements after 4 month resulted in slightly different fat fraction values than the initial measurements but mostly the changes are within the σ inside the evaluated region. Probably the emulsions were not perfectly homogeneous from the beginning and a different slice was measured at the second measurement or the emulsions with high fat content changed (macroscopically not visible) over time and therefore the fat fraction rose. Due to the fact that the $100\%_{vol}$ result differed by more than two σ, the used fat model also can be a reason for the variations. The fat model from [19] is only an approximation. If there is only a slight deviation a small amount of the fat signal is falsely indicated as water signal. To distinguish whether there is a real change in fat fractions over time or the reason for the changes can be found in repeatability issues, a larger set of measurements would be needed for the initial fat fraction evaluation as well as for the measurements after four month.

4.5 Magnetization Transfer Phantoms

The created MT phantoms still have some air bubbles enclosed and therefore for future phantoms it can be recommended to prepare less of the ovalbumin solution at once since foaming was less prevalent for smaller amounts.

In earlier works [78] a relation between Gd-DTPA relaxivity and protein concentration is described. Since this relationship was not taken into consideration when the phantoms were created the difference between adjusted and real values could be described with that relation. The resulting relaxation times are low when compared to tissue relevant relaxation times (see Table 2.1).

The bound pool fraction measured for the created phantoms (see Table 3.7) is in a range that is comparable to the results found in the literature for bovine serum albumin [47] and also to bound pool fractions that can be measured in tissue [47]. The variation of f in the mentioned table can be explained by the slightly varying treatment of the different phantoms in order to get rid of the foam that formed during creation process. The first defoaming method that was tried was freezing and thawing the ovalbumin dilutions. This process was not examined on all the phantoms for equally many cycles. Especially MT-3 and MT-5 experienced more freeze thawing cycles than the other phantoms and MT-6, MT-7 and MT-8 experienced less than half of the freeze thaw cycles the other phantoms were exposed to. It is known that freeze thaw cycles on proteins can denaturate proteins in multiple ways [79]. Therefore the resulting bound pool fraction variations are plausible.

The rapid T_1 quantification overestimates the T_1 values for the MT phantoms. In Figure 3.14 it can be seen that there may be a relation between bound pool fraction and the rapid T_1 quantification which is probably due to the relation of steady state imaging methods and MT effects that is described in literature [80]. Anyway further investigations are necessary for more precise statements on the impact of MT effects on the presently used T_1

quantification method.

In terms of stability the created phantoms seem to stay constant with respect to their relaxation times. The discrepancy in the MT-5 phantom may be due to a general inhomogeneity of this phantom, which can also be seen in it's large σ. Probably the selected slice was not at the same location for the two measurements.

4.6 Conclusion

It can be concluded that an extensible phantom system was created that has three different phantom types that in general meet their requirements with respect to the desired parameters of each phantom type. With the addition of stearic acid to a fat water phantom recipe that has been described in literature in similar ways multiple times [41, 7, 44] the creation of stable phantoms even for the high fat concentrations was enabled. Further for the creation of MT effects with the utilization of ovalbumin a substantially cheaper alternative to the commonly used bovine serum albumin was found. Even though further improvements can be made regarding the trapped air in relaxation phantoms and the homogeneity in the MT phantoms.

Bibliography

[1] N. A. Obuchowski, A. P. Reeves, et al. : Quantitative imaging biomarkers: A review of statistical methods for computer algorithm comparisons. *Stat. Methods. Med. Res.* 24.1 (2015), 68–106. ISSN: 0962-2802. DOI: 10.1177/0962280214537390.

[2] K. E. Keenan, M. Ainslie, et al. : Quantitative magnetic resonance imaging phantoms: A review and the need for a system phantom. *Magn. Reson. Med* 79.1 (2018), 48–61. ISSN: 1522-2594. DOI: 10.1002/mrm.26982.

[3] Jean-Marie Bonny. "Methods and Applications of Quantitative MRI." In: *Annual Reports on NMR Spectroscopy*. Ed. by G. A. Webb. Vol. 56. Academic Press, 2005, 213–229. DOI: 10.1016/S0066-4103(05)56004-6.

[4] P. S. Tofts. : Concepts: Measurement and MR. In: *Quantitative MRI of the Brain*. Wiley-Blackwell, 2004. Chap. 1, pp. 1–15. ISBN: 9780470869529. DOI: 10.1002/0470869526.ch1.

[5] P. A. Gowland and V. L. Stevenson. : T1: The Longitudinal Relaxation Time. In: *Quantitative MRI of the Brain*. Wiley-Blackwell, 2004. Chap. 5, pp. 111–141. ISBN: 9780470869529. DOI: 10.1002/0470869526.ch5.

[6] P. A. Boulby and F. J. Rugg-Gunn. : T2: The Transverse Relaxation Time. In: *Quantitative MRI of the Brain*. Ed. by P. Tofts. Wiley-Blackwell, 2004. Chap. 6, pp. 143–201. ISBN: 9780470869529. DOI: 10.1002/0470869526.ch6.

[7] C. D. G. Hines, H. Yu, et al. : T1 independent, T2* corrected MRI with accurate spectral modeling for quantification of fat: Validation in a fat-water-SPIO phantom. *J. Magn. Reson. Imaging* 30.5 (2009), 1215–1222. ISSN: 1522-2586. DOI: 10.1002/jmri.21957.

[8] P. S. Tofts. : QA: Quality Assurance, Accuracy, Precision and Phantoms. In: *Quantitative MRI of the Brain*. John Wiley and Sons, Ltd, 2004, pp. 55–81. DOI: 10.1002/0470869526.ch3.

[9] : The Phantom Laboratory. 2017. URL: https://www.phantomlab.com/ (visited on 10/28/2018).

[10] : Leeds Test Objects. 2018. URL: http://www.leedstestobjects.com/ (visited on 10/28/2018).

[11] Z. Gimbutas, A. Dienstfrey, et al. : Quantitative MRI: Standards, Analysis Tools, and Algorithms. URL: https://collaborate.nist.gov/mriphantoms/bin/view/MriPhantoms/WebHome (visited on 10/28/2018).

[12] : NIST MRI Phantoms. URL: https://collaborate.nist.gov/mriphantoms/bin/view/MriPhantoms/WebHome (visited on 10/28/2018).

[13] *American College of Radiology MR Accreditation Program Testing Instructions*. American College of Radiology. 2017. URL: https://www.acraccreditation.org/-/media/ACRAccreditation/Documents/MRI/MRAccreditationTestingInstructions.pdf?la=en.

[14] E. F. Jackson, M. J. Bronskill, et al. *Acceptance Testing and Quality Assurance Procedures for Magnetic Resonance Imaging Facilities*. Tech. rep. American Association of Physicists in Medicine, (2010).

[15] : NIST MRI Phantoms. URL: https://www.nist.gov/news-events/news/2010/05/meet-phannie-nists-standard-phantom-calibrating-mri-machines (visited on 01/15/2018).

[16] : ACR MRI Phantoms. URL: https://www.newmaticmedical.com/phantom/p/ACRMRIPhantom/ (visited on 01/15/2018).

[17] X. Ou and D. F. Gochberg. : MT Effects and T(1) Quantification in Single-Slice Spoiled Gradient Echo Imaging. *Mag. Reson. Med.* 59.4 (2008), 835–845. ISSN: 1522-2594. DOI: 10.1002/mrm.21550.

[18] M. D. Robson, S. K. Piechnik, et al. : T1 measurements in the human myocardium: The effects of magnetization transfer on the SASHA and MOLLI sequences. *Magn. Reson. Med.* 70.3 (2013), 664–670. ISSN: 1522-2594. DOI: 10.1002/mrm.24867.

[19] A. Lesch, K. Bredies, et al., eds. *Chemical Shift based Fat-Water Separation using a Variational Approach for Bo-field Correction*. Vol. In Proceedings of the 24th Annual Meeting of ISMRM, Singapore, 2016; p. 4284. (2016).

[20] V. Siracusa. : Food Packaging Permeability Behaviour: A Report. *International Journal of Polymer Science* 2012 (2012). DOI: 10.1155/2012/302029.

[21] B. P. Kremer and H. Bannwarth. *Werkstoffe, Geräte, Apparaturen*. Berlin, Heidelberg: Springer, (2014), pp. 35–48. DOI: 10.1007/978-3-642-54334-0_3.

[22] : Liquid Degassing and Deaeration. URL: http://sonomechanics.com/applications/liquid_degassing/ (visited on 10/28/2018).

[23] K. Yoshimura, H. Kato, et al. : Development of a tissue-equivalent MRI phantom using carrageenan gel. *Magn. Reson. Med.* 50.5 (2003), 1011–1017. ISSN: 1522-2594. DOI: 10.1002/mrm.10619.

[24] P. S. Tofts, B. Shuter, et al. : Ni-DTPA doped agarose gel - A phantom material for Gd-DTPA enhancement measurements. *Magn. Reson. Med.* 11.1 (1993), 125–133. ISSN: 0730-725X. DOI: 10.1016/0730-725x(93)90420-i.

[25] K. Thangavel and E. U. Saritas. : Aqueous paramagnetic solutions for MRI phantoms at 3 T:A detailed study on relaxivities. *Turk. J. Elec. Eng. & Comp. Sci.* 25 (2017), 2108–2121. DOI: 10.3906/elk-1602-123.

[26] G. J. Stanisz, E. E. Odrobina, et al. : T1, T2 relaxation and magnetization transfer in tissue at 3T. *Magn. Reson. Med.* 54.3 (2005), 507–512. ISSN: 1522-2594. DOI: 10.1002/mrm.20605.

[27] S. Ohno, H. Kato, et al. : Production of a Human-Tissue-Equivalent MRI Phantom: Optimization of Material Heating: *Magn. Reson. Med. Sci.* 7.3 (2008), 131–140. DOI: 10.2463/mrms.7.131.

[28] K. A. Kraft, P. P. Fatouros, et al. : An MRI phantom material for quantitative relaxometry. *Magn. Reson. Med.* 5.6 (1987), 555–562. ISSN: 1522-2594. DOI: 10.1002/mrm.1910050606.

[29] J.O. Christoffersson, L. Olsson, et al. : Nickel-doped agarose gel phantoms in MR imaging. *Acta Radiol.* 32 (1991), 426–31.

[30] D. Mendelson, J. Filion Heinsbergen, et al. : Comparison of agarose and cross-linked protein gels as magnetic resonance imaging phantoms. *Magn. Reson. Med.* 9 (1991), 975–8. DOI: 10.1016/0730-725X(91)90546-X.

[31] Y. Shen, F. L. Goerner, et al. : T1 Relaxivities of Gadolinium-Based Magnetic Resonance Contrast Agents in Human Whole Blood at 1.5, 3, and 7 T. *Investigative Radiology* 50.5 (2015), 330–338. ISSN: 0020-9996. DOI: 10.1097/RLI.0000000000000132.

[32] J. Z. Bojorquez, S. Bricq, et al. : What are normal relaxation times of tissues at 3 T? *Magn. Reson. Imaging* 35 (2017), 69–80. ISSN: 0730-725X. DOI: 10.1016/j.mri.2016.08.021.

[33] L. O. Morgan and A. W. Nolle. : Proton Spin Relaxation in Aqueous Solutions of Paramagnetic Ions. II. Cr+++, Mn++, Ni++, Cu++, and Gd+++. *J. Chem. Phys.* 31.2 (1959), 365–368. ISSN: 0021-9606. DOI: 10.1063/1.1730360.

[34] I. Solomon and N. Bloembergen. : Nuclear Magnetic Interactions in the HF Molecule. *J. Chem. Phys.* 25.2 (1956), 261–266. ISSN: 0021-9606. DOI: 10.1063/1.1742867.

[35] M. A. Bernstein, K. F. King, et al. "Chapter 16 - Echo Train Pulse Sequences." In: *Handbook of MRI Pulse Sequences*. Burlington: Academic Press, 2004, 702–801. DOI: 10.1016/B978-0-12-092861-3.X5000-6.

[36] U. Harten. "Wärmelehre." In: *Physik: Eine Einführung für Ingenieure und Naturwissenschaftler*. Ed. by Ulrich Harten. Berlin, Heidelberg: Springer, 2014, 135–177. DOI: 10.1007/978-3-642-53854-4_5.

[37] Roger Walker. : Density of Water. 2015. URL: https://www.simetric.co.uk/si_water.htm (visited on 10/28/2018).

[38] T. F. Tadros. : Emulsion Formation, Stability, and Rheology. In: *Emulsion Formation and Stability*. Wiley-VCH Verlag GmbH and Co. KGaA, 2013, pp. 1–75. DOI: 10.1002/9783527647941.ch1.

[39] W. P. Coleman. : Handbook of Cosmetic Science and Technology, 3rd Edition. *Dermatologic Surgery* 36.3 (2010), 769–784. DOI: 10.1111/j.1524-4725.2009.01444.x.

[40] J. L. Knowlton and S. E. M. Pearce. *Handbook of Cosmetic Science and Technology*. 1st ed. Elsevier Advanced Technology, (1993). ISBN: 1-85617-197-3.

[41] C. P. Bernard, G. P. Liney, et al. : Comparison of fat quantification methods: A phantom study at 3.0T. *Magn. Reson. Imaging* 27.1 (2008), 192–197. ISSN: 1522-2586. DOI: 10.1002/jmri.21201.

[42] D. Hernando, Z.-P. Liang, et al. : Chemical Shift-Based Water/Fat Separation: A Comparison of Signal Models. *MAgn. Reson. Med.* 64.3 (2010), 811–822. ISSN: 1522-2594. DOI: 10.1002/mrm.22455.

[43] H. Yu, A. Shimakawa, et al. : Multi-Echo Water-Fat Separation and Simultaneous R2* Estimation with Multi-Frequency Fat Spectrum Modeling. *Magn. Reson. Med.* 60.5 (2008), 1122–1134. ISSN: 1522-2594. DOI: 10.1002/mrm.21737.

[44] D. Hernando, S. D. Sharma, et al. : Multisite, multivendor validation of the accuracy and reproducibility of proton-density fat-fraction quantification at 1.5T and 3T using a fat-water phantom. *Magn. Reson. Med.* 77.4 (2017), 1516–1524. ISSN: 1522-2594. DOI: 10.1002/mrm.26228.

[45] R. M. Henkelman, G. J. Stanisz, et al. : Magnetization transfer in MRI: a review. *NMR Biomed.* 14.2 (2001), 57–64. ISSN: 1099-1492. DOI: 10.1002/nbm.683.

[46] S. H. König, R. D. Brown, et al. : Magnetization transfer in cross-linked bovine serum albumin solutions at 200 MHz: A model for tissue. *Magn. Reson. Med.* 29.3 (1993), 311–316. ISSN: 1522-2594. DOI: 10.1002/mrm.1910290306.

[47] M. Söllinger, C. Langkammer, et al. : Fast Bound Pool Fraction Mapping Using Stimulated Echoes. *Magn. Reson. Med.* 66.3 (2010), 717–724. ISSN: 1522-2594. DOI: 10.1002/mrm.22846.

[48] R. W. Brown, Y.-C. N. Cheng, et al. *Magnetic Resonance Imaging: Physical Principles and Sequence Design*. 2nd ed. Hoboken, NJ: Wiley Blackwell, (2014). DOI: 10.1002/9781118633953.

[49] Z.-P. Liang and P. C. Lauterbur. "Signal Characteristics." In: *Principles of Magnetic Resonance Imaging: A Signal Processing Perspective*. Wiley-IEEE Press, 2000. Chap. 4, 416. DOI: 10.1109/9780470545652.ch4.

[50] P. Jezzard and R. S. Balaban. : Correction for geometric distortion in echo planar images from Bo field variations. *Magn. Reson. Med.* 34.1 (2005), 65–73. ISSN: 0740-3194. DOI: 10.1002/mrm.1910340111.

[51] S. Chavez, Q.-S. Xiang, et al. : Understanding phase maps in MRI: a new cutline phase unwrapping method. *IEEE Trans. Med. Imaging* 21.8 (2002), 966–977. ISSN: 0278-0062. DOI: 10.1109/TMI.2002.803106.

[52] B. Spottiswoode. : 2D phase unwrapping algorithms. 2009. URL: https://www.mathworks.com/matlabcentral/fileexchange/22504-2d-phase-unwrapping-algorithms (visited on 10/28/2018).

[53] O. Maier, J. Schoormans, et al. : Rapid T1 quantification from high resolution 3D data with model-based reconstruction. *Magn Reson Med.* (2018). DOI: 10.1002/mrm.27502.

[54] L. I. Sacolick, F. Wiesinger, et al. : B(1) Mapping by Bloch-Siegert Shift. *Magn. Reson. Med.* 63.5 (2010), 1315–1322. ISSN: 1522-2594. DOI: 10.1002/mrm.22357.

[55] A. Lesch, M. Schlögl, et al. : Ultrafast 3D Bloch-Siegert B1+-Mapping using Variational Modeling. *Magn. Reson. Med.* (2018), 00:1–12. DOI: 10.1002/mrm.27434.

[56] D. W. McRobbie, E. A. Moore, et al. *MRI from Picture to Proton*. 2nd ed. Cambridge: Cambridge University Press, (2006). DOI: 10.1017/cbo9780511545405.

[57] N. Ben-Eliezer, D. K. Sodickson, et al. : Rapid and Accurate T2 Mapping from Multi Spin Echo Data Using Bloch-Simulation-Based Reconstruction. *Magn. Reson. Med.* 73.2 (2014), 809–817. ISSN: 1522-2594. DOI: 10.1002/mrm.25156.

[58] P. Kellman, D. A. Herzka, et al. : Adiabatic inversion pulses for myocardial T1 mapping. *Magn. Reson. Med.* 71.4 (2014), 1428–1434. ISSN: 0740-3194. DOI: 10.1002/mrm.24793.

[59] Jozef Kowalewski, George C Levy, et al. : A three-parameter non-linear procedure for fitting inversion-recovery measurements of spin-lattice relaxation times. *J. Magn. Reson.* 26.3 (1977), 533–536. ISSN: 0022-2364. DOI: 10.1016/0022-2364(77)90106-8.

[60] R. A. Bernheim, T. H. Brown, et al. : Temperature Dependence of Proton Relaxation Times in Aqueous Solutions of Paramagnetic Ions. *J. Chem. Phys.* 30.4 (1959), 950–956. ISSN: 0021-9606. DOI: 10.1063/1.1730133.

[61] O. Dössl. *Bildgebende Verfahren in der Medizin*. 2nd ed. Springer, (2016). DOI: 10.1007/978-3-642-54407-1.

[62] D. Stefan, F. Di Cesare, et al. : Quantitation of magnetic resonance spectroscopy signals: the jMRUI software package. *Meas. Sci. Technol.* 20.10 (2009), 104035. ISSN: 0957-0233. DOI: 10.1088/0957-0233/20/10/104035.

[63] A. Naressi, C. Couturier, et al. : Java-based graphical user interface for MRUI, a software package for quantitation of in vivo/medical magnetic resonance spectroscopy signals. *Comput. Biol. Med.* 31.4 (2001), 269–286. ISSN: 0010-4825. DOI: 10.1016/S0010-4825(01)00006-3.

[64] L. Vanhamme, A. van den Boogaart, et al. : Improved Method for Accurate and Efficient Quantification of MRS Data with Use of Prior Knowledge. *J. Magn. Reson.* 129.1 (1997), 35–43. ISSN: 1090-7807. DOI: 10.1006/jmre.1997.1244.

[65] W. T. Dixon. : Simple proton spectroscopic imaging. *Radiology* 153.1 (1984), 189–194. ISSN: 0033-8419. DOI: 10.1148/radiology.153.1.6089263.

[66] Glover G. H. : Multipoint dixon technique for water and fat proton and susceptibility imaging. *J. Magn. Reson. Imaging* 1.5 (1991), 521–530. DOI: 10.1002/jmri.1880010504. eprint: https://onlinelibrary.wiley.com/doi/pdf/10.1002/jmri.1880010504.

[67] Reeder S.B., Wen Z., et al. : Multicoil Dixon chemical species separation with an iterative least squares estimation method. *Magn. Reson. Med.* 51.1 (2004), 35–45. DOI: 10.1002/mrm.10675. eprint: https://onlinelibrary.wiley.com/doi/pdf/10.1002/mrm.10675.

[68] S. B. Reeder, C. A. McKenzie, et al. : Water-fat separation with IDEAL gradient-echo imaging. *J. Magn. Reson. Imaging* 25.3 (2007), 644–652. ISSN: 1522-2586. DOI: 10.1002/jmri.20831.

[69] S. B. Reeder, C. D. Hines, et al., eds. *On the definition of fat-fraction for in vivo fat quantification with magnetic resonance imaging.* Vol. Proceedings of the 17th annual meeting of ISMRM. ISMRM, (2009).

[70] : Pubchem. URL: https://pubchem.ncbi.nlm.nih.gov/ (visited on 10/28/2018).

[71] J. Orsavova, L. Misurcova, et al. : Fatty Acids Composition of Vegetable Oils and Its Contribution to Dietary Energy Intake and Dependence of Cardiovascular Mortality on Dietary Intake of Fatty Acids. *Int. J. Mol. Sci.* 16.6 (2015). ISSN: 1422-0067. DOI: 10.3390/ijms160612871.

[72] University of Idaho. : Triglyceride Molecular weight calculator. 2017. URL: http://biodieseleducation.org/Production/MolecularWeightCalculator.html (visited on 10/28/2018).

[73] J.-F. Cabana, Y. Gu, et al. : Quantitative magnetization transfer imaging made easy with qMTLab: Software for data simulation, analysis, and visualization. *Concepts Magn. Reson.* 44A.5 (2015), 263–277. ISSN: 1546-6086. DOI: 10.1002/cmr.a.21357.

[74] V. Yarnykh. : Mathematical modeling of the magnetization transfer effect in tissues. *J. Phys.: Conference Series* 677.1 (2016), 012001. ISSN: 1742-6596. DOI: 10.1088/1742-6596/677/1/012001.

[75] G.J. Barker, P.S. Tofts, et al. : An interleaved sequence for accurate and reproducible clinical measurement of Magnetization Transfer Ratio. *Magn. Reson. Imaging* 14.4 (1996), 403–411. ISSN: 0730-725X. DOI: 10.1016/0730-725X(96)00019-7.

[76] J. Kruisz, A. Petrovic, et al., eds. *Investigation of temperature dependence of tissue relaxation parameters for post-mortem imaging*. 21 2469. Int. Soc. Mag. Reson. Med., (2013).

[77] V. S. Vassiliou, E. L. Heng, et al. : Magnetic resonance imaging phantoms for quality-control of myocardial T1 and ECV mapping: specific formulation, long-term stability and variation with heart rate and temperature. *Journal of Cardiovascular Magnetic Resonance* 18.1 (2016), 62. ISSN: 1532-429X. DOI: 10.1186/s12968-016-0275-9.

[78] G. J. Stanisz and R. M. Henkelman. : Gd-DTPA relaxivity depends on macromolecular content. *Magn. Reson. Med.* 44.5 (2000), 665–667. ISSN: 1522-2594. DOI: 10.1002/1522-2594(200011)44:5<665::AID-MRM1>3.0.CO;2-M.

[79] U. T. Lashmar, M. Vanderburgh, et al. *Bulk Freeze-Thawing of Macromolecules - Effects of Cryoconcentration on Their Formulation and Stability*. Tech. rep. Bioprocess International, (2007). URL: https://www.sartorius.com/_ui/images/h2a/hef/8878708719646.pdf.

[80] O. Bieri and K. Scheffler. : On the origin of apparent low tissue signals in balanced SSFP. *Magn. Reson. Med.* 56.5 (2006), 1067–1074. ISSN: 0740-3194. DOI: 10.1002/mrm.21056.

Appendix

Appendix A

Technical Drawings Housing

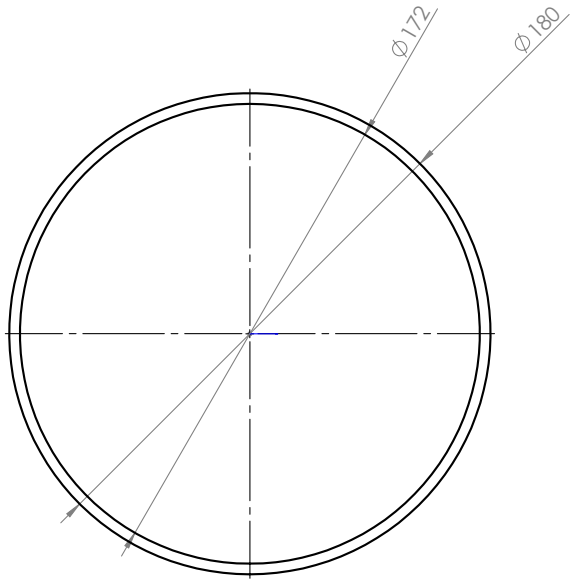

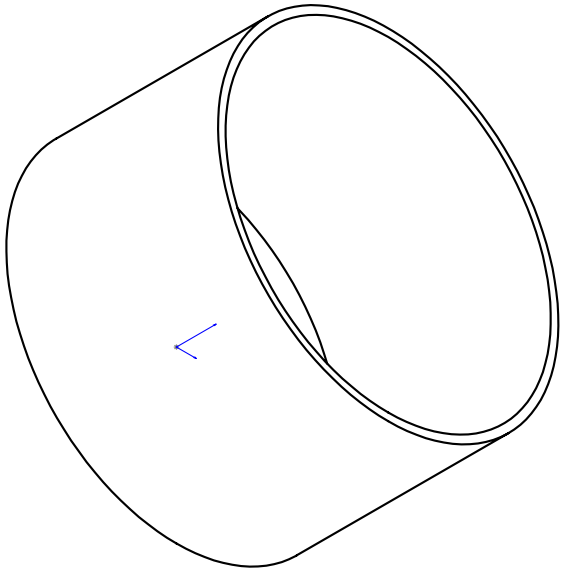

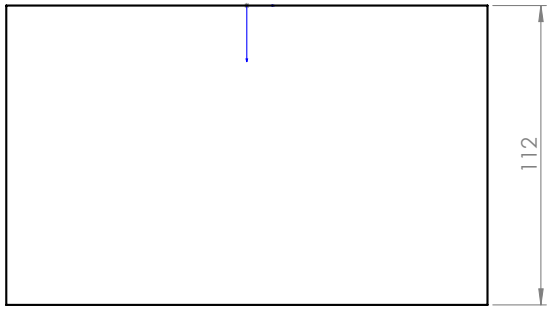

WÄRMEBEHANDLUNG		OBERFLÄCHE		MASSTAB	1:2
MATERIAL	Acryl (halb- bis hochschlagzäh) 180x112	KUNDE	TU GRAZ		
			DATUM	NAME	BEZEICHNUNG
		ERSTELLT	16.01.2019	RieT	PHM_Acrylic Tube
		FREIGABESTATUS (gültig m. ausgefülltem Feld)			
		PROTOTYP	.	.	
		SERIE			
		FREIMASSTOLERANZ	DIN2768 mittel	Werkstückkanten nach DIN6784 -0,2 +0,4	ZEICHNUNGSNUMMER I0000A0
					FORMAT A3
	10.05.2018				Blatt 1 / 1
INDEX ÄNDERUNG	DATUM	NAME	Schutzvermerk nach DIN 34 beachten	Druckdatum: 16.01.2019	Ersatz für:

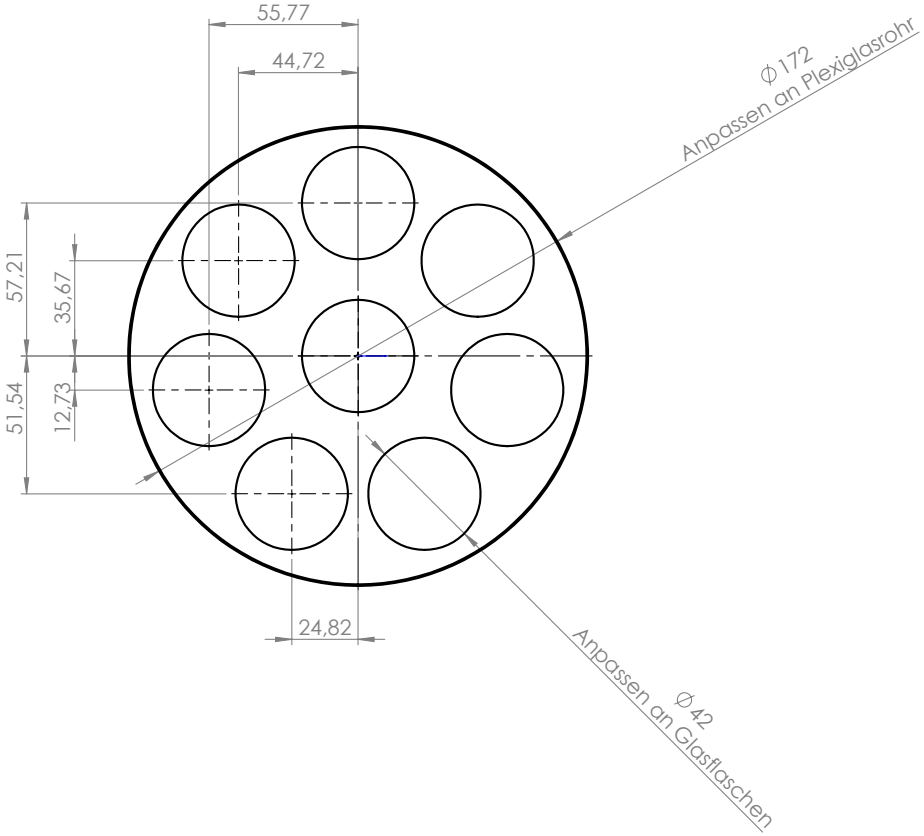

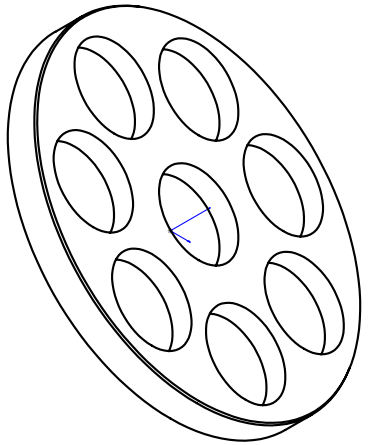

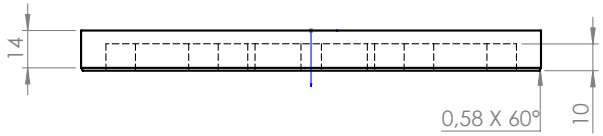

WÄRMEBEHANDLUNG			OBERFLÄCHE		MASSTAB	1:2	
MATERIAL	PA Typ 6	172x15	KUNDE	TU Graz			
				DATUM	NAME	BEZEICHNUNG	PHM_Bottom
			ERSTELLT	16.01.2019	RieT		
			FREIGABESTATUS (gültig m. ausgefülltem Feld)				
			PROTOTYP	.	.		
			SERIE				
			FREIMASSTOLERANZ	DIN2768 mittel	Werkstückkanten nach DIN6784 -0,2 +0,4	ZEICHNUNGSNUMMER	I0A001A
						FORMAT	A3
							Blatt 1 / 1
INDEX	ÄNDERUNG	DATUM	NAME	Schutzvermerk nach DIN 34 beachten		Druckdatum: 16.01.2019	Ersatz für:

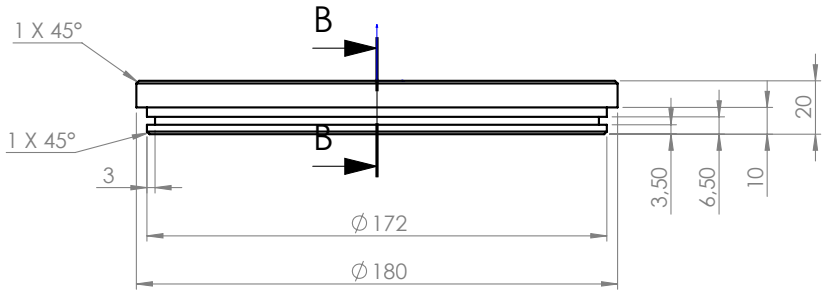

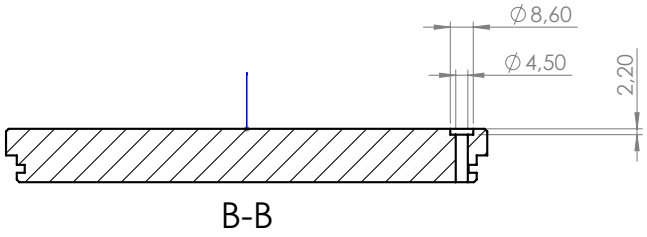

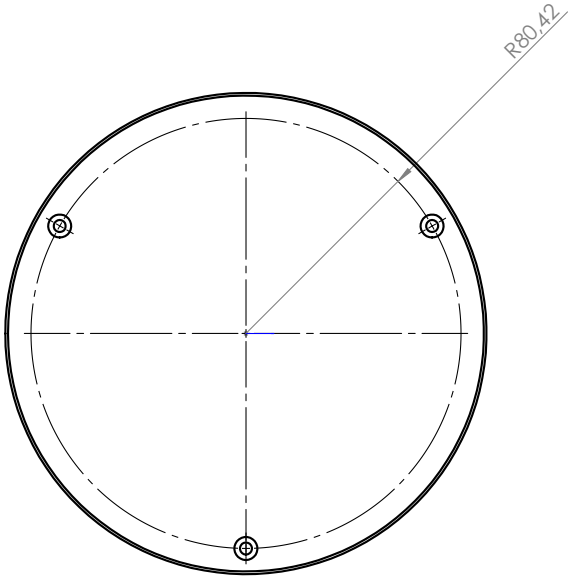

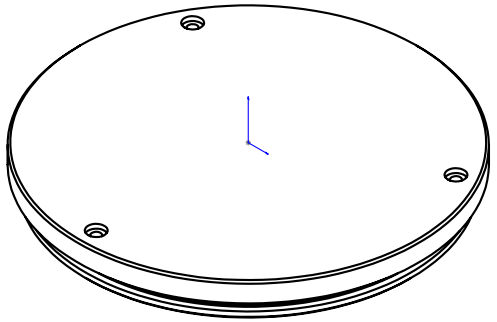

WÄRMEBEHANDLUNG			OBERFLÄCHE		MASSTAB 1:2		
MATERIAL PA Typ 6		180x22	KUNDE TU Graz				
				DATUM	NAME	BEZEICHNUNG PHM_Top	
			ERSTELLT	16.01.2019	RieT		
			FREIGABESTATUS (gültig m. ausgefülltem Feld)				
			PROTOTYP	.	.		
			SERIE				
			FREIMASSTOLERANZ DIN2768 mittel	Werkstückkanten nach DIN6784 -0,2 +0,4		ZEICHNUNGSNUMMER I0A003A0	FORMAT A3
							Blatt 1/1
INDEX	ÄNDERUNG	DATUM	NAME	Schutzvermerk nach DIN 34 beachten		Druckdatum: 16.01.2019	Ersatz für:

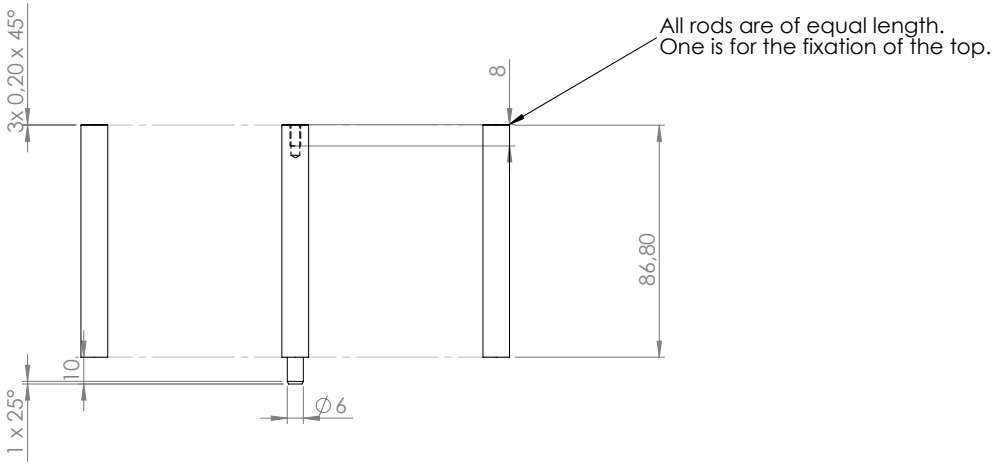

WÄRMEBEHANDLUNG			OBERFLÄCHE		MASSTAB 1:1	
MATERIAL PA Typ 6			KUNDE TU Graz			
				DATUM	NAME	BEZEICHNUNG PHM_Rods
			ERSTELLT	16.01.2019	RieT	
			FREIGABESTATUS (gültig m. ausgefülltem Feld)			
			PROTOTYP	.	.	
			SERIE			
			FREIMASSTOLERANZ DIN2768 mittel	Werkstückkanten nach DIN6784 -0,2 +0,4		ZEICHNUNGSNUMMER I0A008A0
INDEX	ÄNDERUNG	DATUM	NAME	Schutzvermerk nach DIN 34 beachten		Druckdatum: 16.01.2019 Ersatz für:

FORMAT A3 Blatt 1/1

Appendix A Technical Drawings Housing

Appendix B

Technical Documentation Homogenizer

B.1 High Shear Mixing Attachment

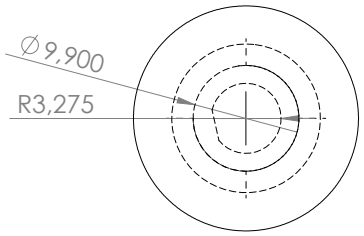

DETAIL J
MAßSTAB 2 : 1

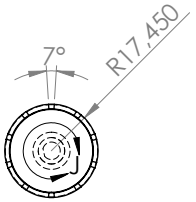

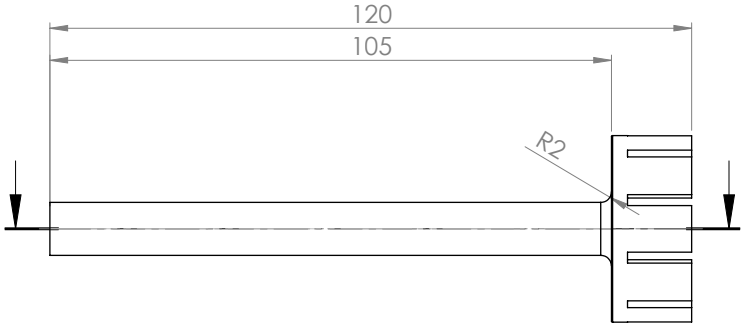

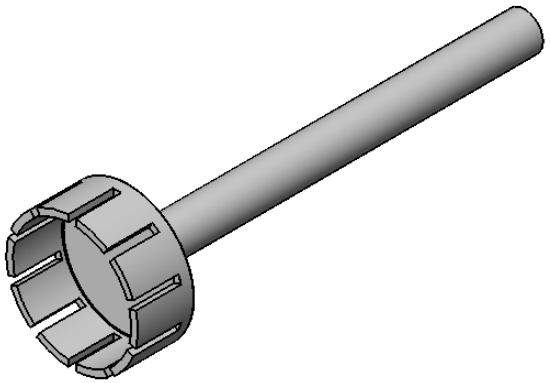

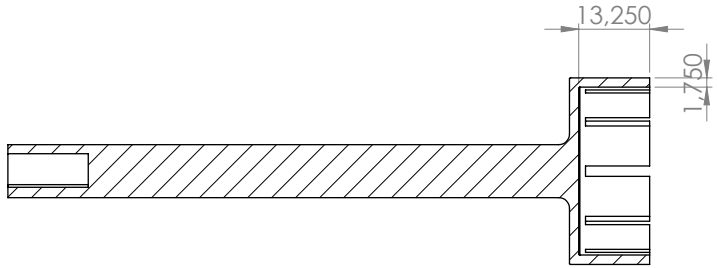

SCHNITT -
MAßSTAB 1 : 1

WÄRMEBEHANDLUNG			OBERFLÄCHE		MASSTAB 1:2		
MATERIAL PLA			KUNDE				
				DATUM	NAME	BEZEICHNUNG Rotor	
			ERSTELLT				
			FREIGABESTATUS (gültig m. ausgefülltem Feld)				
			PROTOTYP	.	.		
			SERIE				
			FREIMASSTOLERANZ DIN2768 mittel	Werkstückkanten nach DIN6784 -0,2 +0,4		ZEICHNUNGSNUMMER I0A006A0	FORMAT A3
							Blatt 1 / 1
INDEX	ÄNDERUNG	DATUM	NAME	Schutzvermerk nach DIN 34 beachten		Druckdatum: 16.01.2019	Ersatz für:

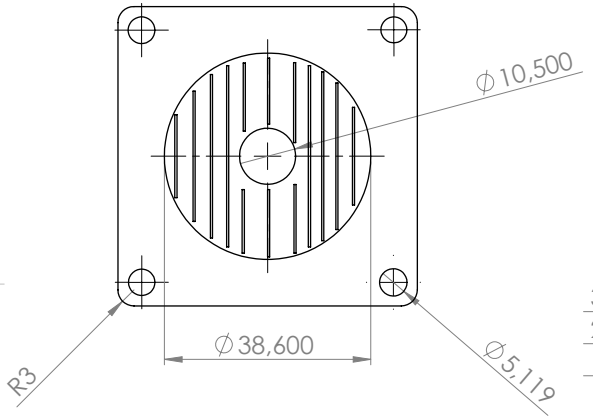

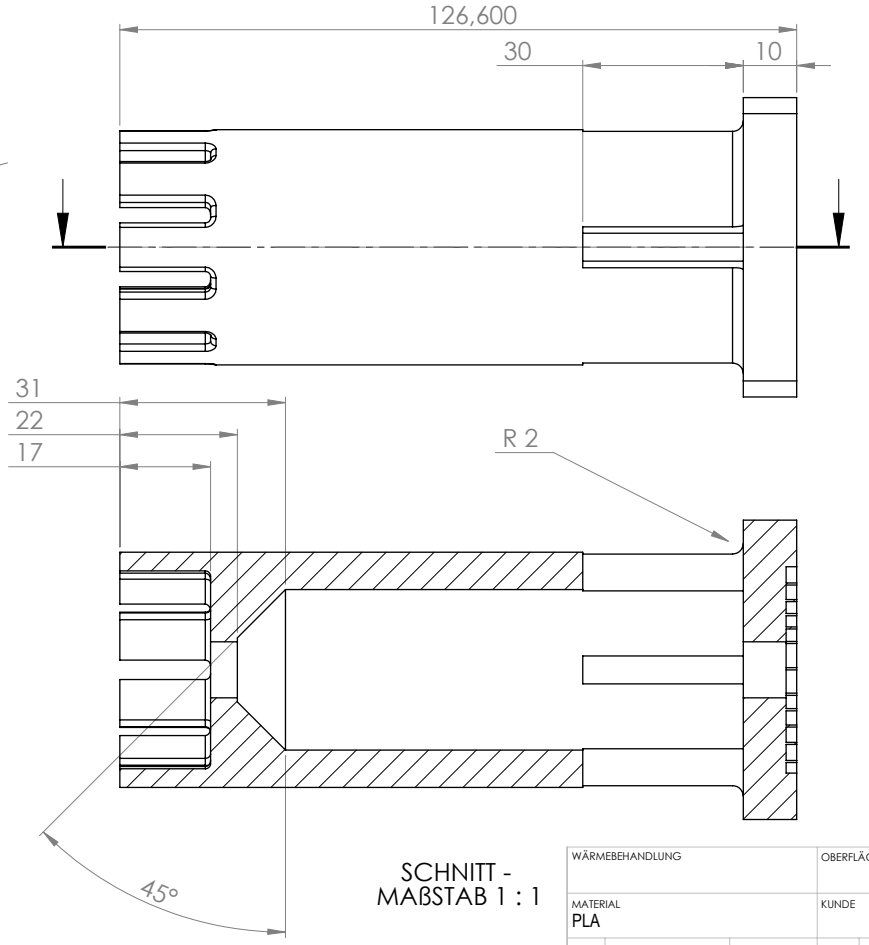

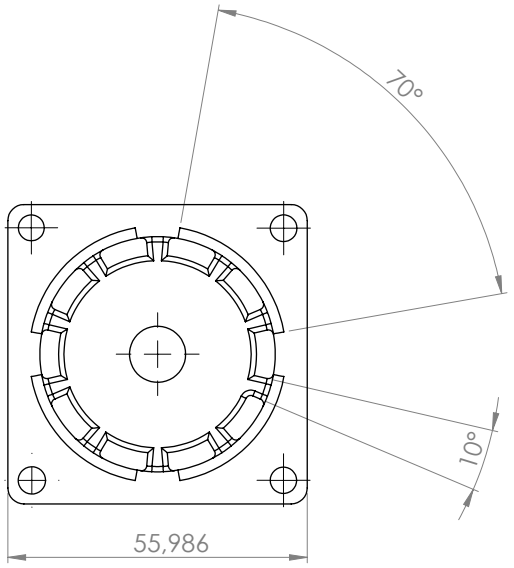

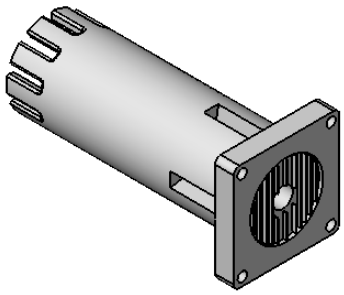

SCHNITT -
MAßSTAB 1 : 1

WÄRMEBEHANDLUNG		OBERFLÄCHE		MASSTAB	1:2
MATERIAL	PLA	KUNDE			
			DATUM	NAME	BEZEICHNUNG: Stator
			ERSTELLT		
			FREIGABESTATUS (gültig m. ausgefülltem Feld)		
			PROTOTYP	.	.
			SERIE		
			FREIMASSTOLERANZ DIN2768 mittel	Werkstückkanten nach DIN6784 -0,2 +0,4	ZEICHNUNGSNUMMER I0A007A0
INDEX	ÄNDERUNG	DATUM	NAME	Schutzvermerk nach DIN 34 beachten	Druckdatum: 16.01.2019 Ersatz für:

FORMAT A3
Blatt 1 / 1

B.2 Motor Control Unit

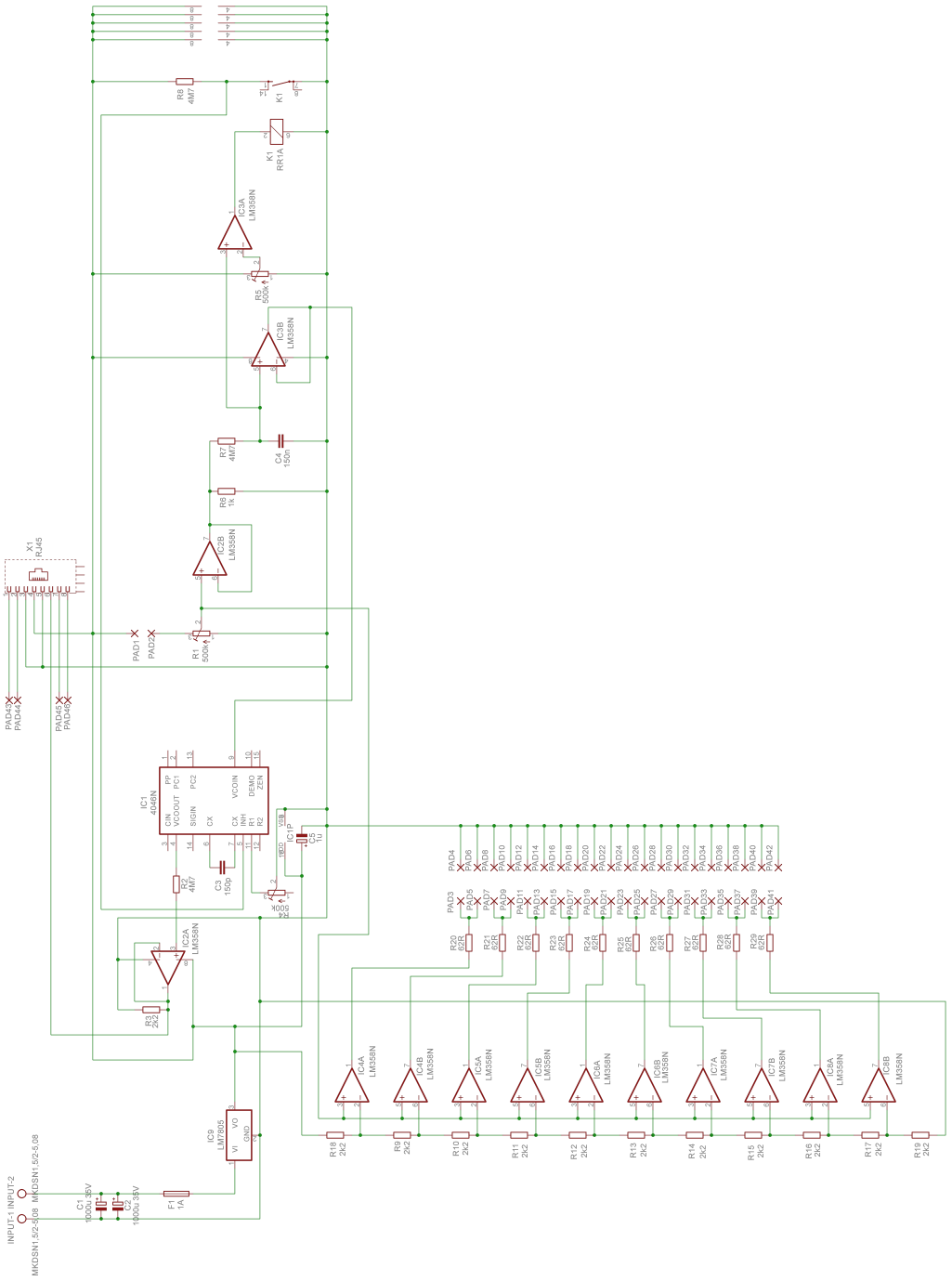

Figure B.1: Schematics of motor control unit

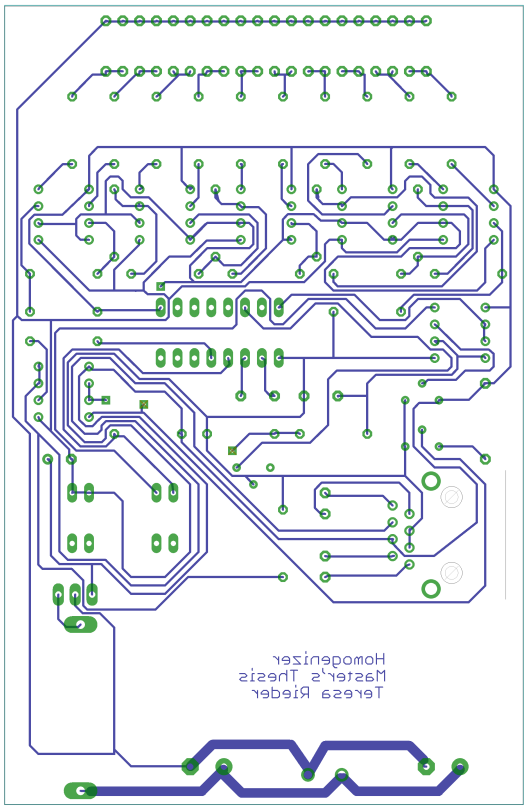

a: Bottom

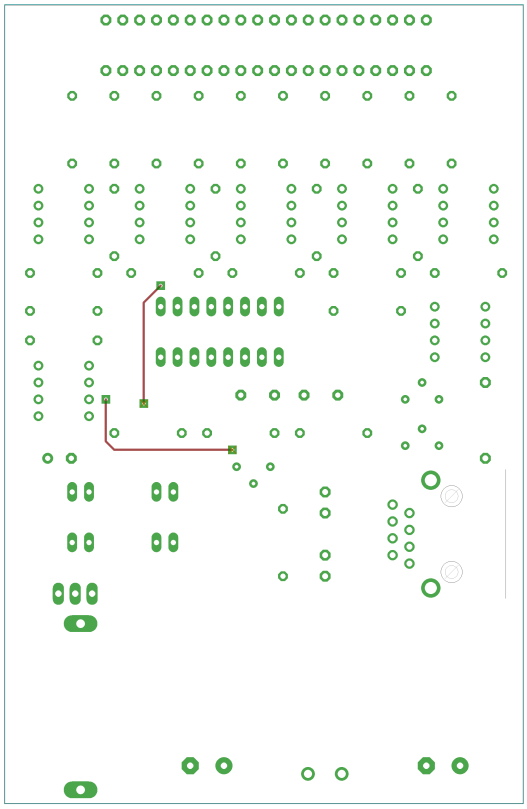

b: Top

Figure B.2: Board layout

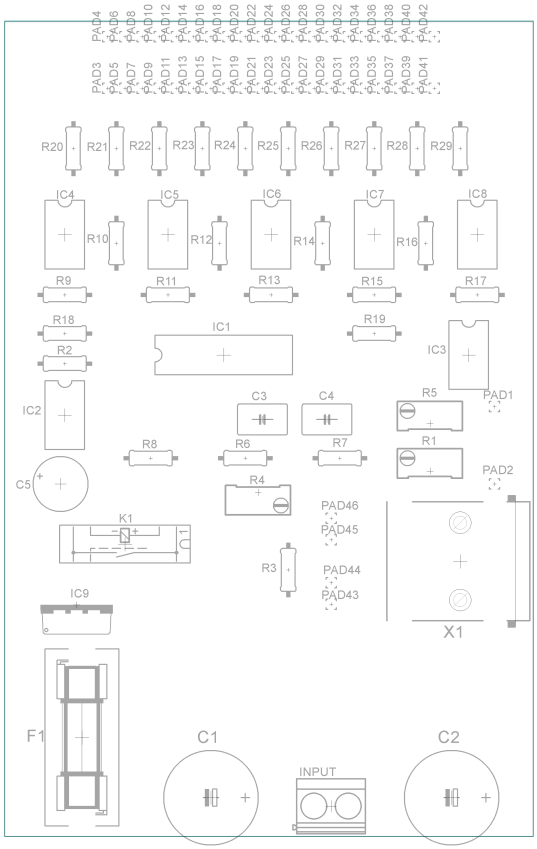

Figure B.3: Assembly plan for the circuit board

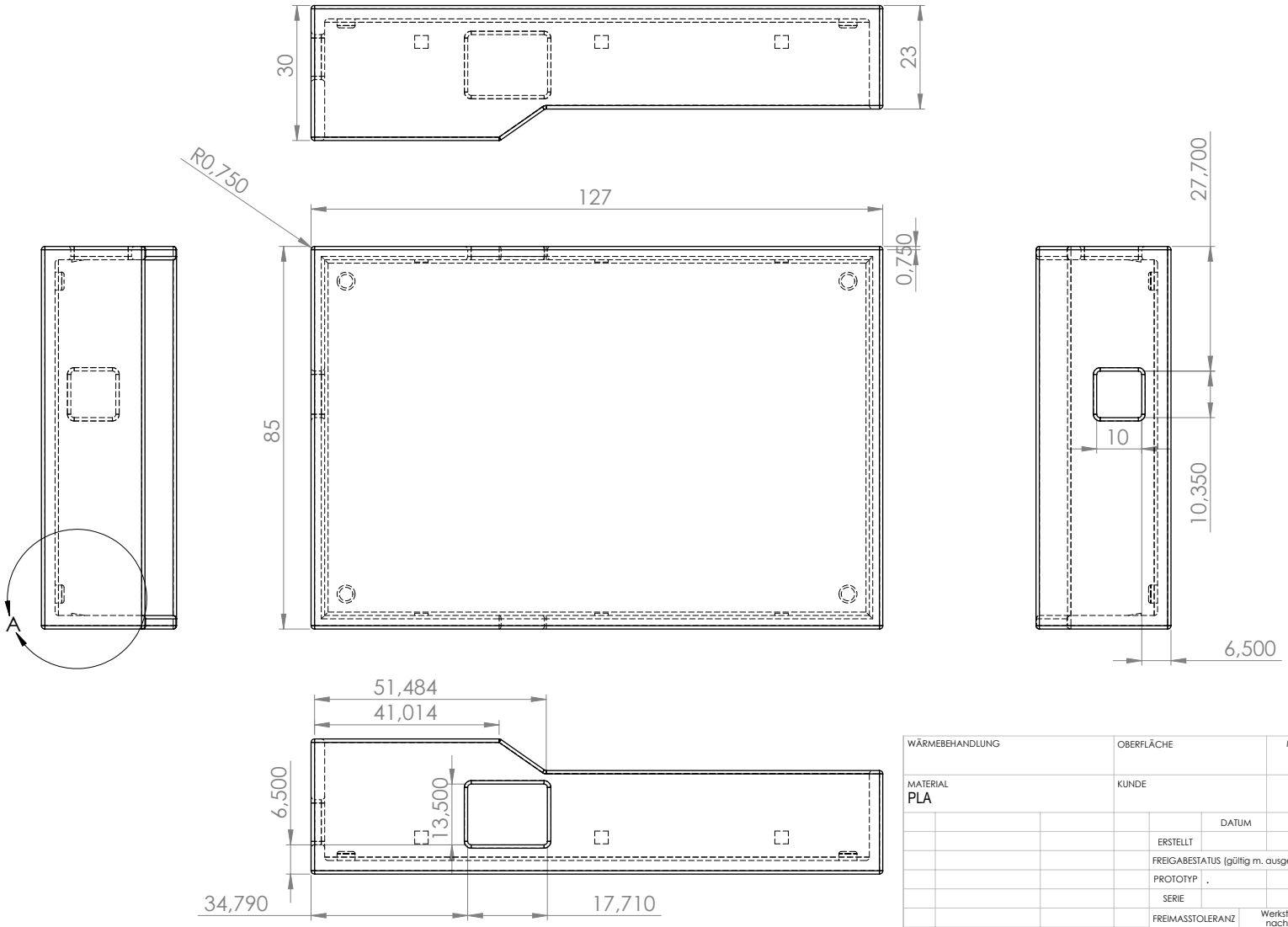

WÄRMEBEHANDLUNG		OBERFLÄCHE		MASSTAB 1:2	
MATERIAL PLA		KUNDE			
			DATUM	NAME	BEZEICHNUNG Board Housing Bottom
		ERSTELLT			
		FREIGABESTATUS (gültig m. ausgefülltem Feld)			
		PROTOTYP	.	.	
		SERIE			
		FREIMASSTOLERANZ DIN2768 mittel	Werkstückkanten nach DIN6784 -0,2 +0,4		ZEICHNUNGSNUMMER I0A004A0
INDEX ÄNDERUNG	DATUM	NAME	Schutzvermerk nach DIN 34 beachten	Druckdatum: 16.01.2019	Ersatz für:

FORMAT A3 Blatt 1/1

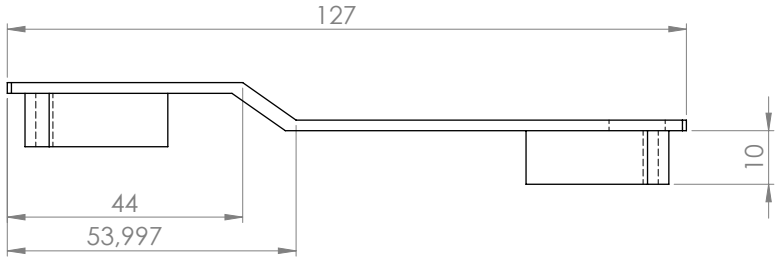

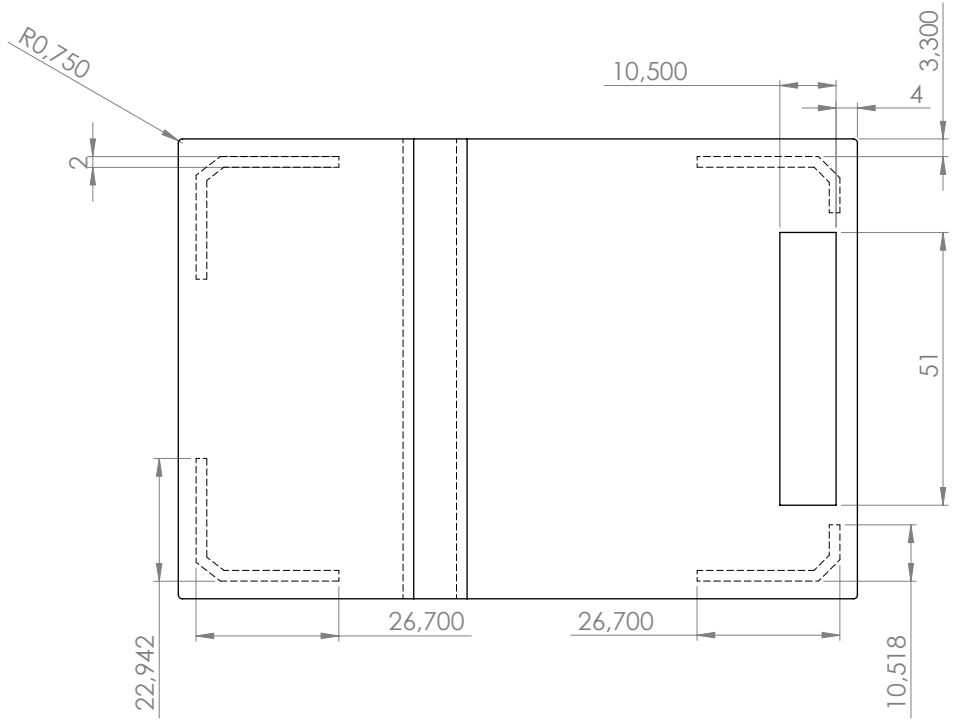

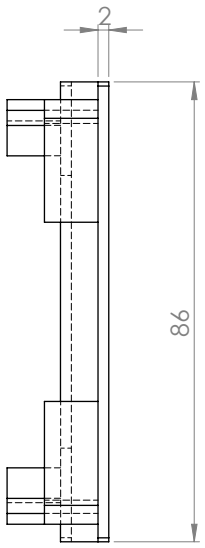

WÄRMEBEHANDLUNG		OBERFLÄCHE		MASSTAB	1:2
MATERIAL	PLA	KUNDE			
			DATUM	NAME	BEZEICHNUNG
		ERSTELLT			Board Housing Top
		FREIGABESTATUS (gültig m. ausgefülltem Feld)			
		PROTOTYP	.	.	
		SERIE			
		FREIMASSTOLERANZ	DIN2768 mittel	Werkstückkanten nach DIN6784 -0,2 +0,4	ZEICHNUNGSNUMMER I0A005A0
					FORMAT A3
					Blatt 1 / 1
INDEX	ÄNDERUNG	DATUM	NAME	Schutzvermerk nach DIN 34 beachten	Druckdatum: 16.01.2019 Ersatz für: